Study on Convective Boundary Layer and Cumulus Clouds over Humid Terrestrial Area
(湿潤な陸域における対流境界層と積雲に関する研究)

Satoshi Endo

(遠藤 智史)

A dissertation for the degree of Doctor of Science

Department of Earth and Environmental Sciences,

Graduate School of Environmental Studies, Nagoya University

(名古屋大学大学院 環境学研究科 地球環境科学専攻 学位論文 博士 (理学))

2009

Abstract

Atmospheric boundary layer functions to carry and store water vapor, which is important for the initiation and development of the deep cumulus convection. Although extensive studies of the convective boundary layer have been conducted for the humid tropical oceans and the relatively dry plains of North America, few studies were conducted for the humid terrestrial area characterized by the small Bowen ratio and strong diurnal variation of large surface fluxes. The purpose of this study is to clarify the development of the dry convective boundary layer and cumulus boundary layer over a humid terrestrial area, the Huaihe River Basin in China.

Data were collected in early summer 2004 using a 32-m flux tower and a 1290-MHz wind profiler radar. When mature wheat fields or bare fields dominated (the first period), the sensible heat flux from the land surface was nearly equal to the latent heat flux. After vegetation changed to paddy fields (the second period), the latent heat flux was much larger than the sensible heat flux. To study the development of dry convective boundary layer, two clear days (31 May and 22 June) were selected from the first and second periods and are referred to as the dry-case and wet-case, respectively. For the dry-case, a deep convective boundary layer developed rapidly from the early morning, and vigorous thermal updrafts dominates. For the wet-case, a shallow convective boundary layer developed slowly from late morning, and thermals were weak. To study the thermodynamic process in the convective boundary layer, high-resolution numerical simulations were conducted. For the dry-case, heat flux contributed to nearly all of buoyancy flux. In contrast, for the wet-case, heat and moisture fluxes made equal contributions. The large contribution of moisture flux to the buoyancy flux is one of the main characteristics of the convective boundary layer over humid

terrestrial areas.

The development of the cumulus boundary layer is investigated using the idealized high-resolution numerical simulations with the focus on the onset of “ active cumulus ”. The parameters of initial profile and the land surface for control experiment were based on the observational data on 20 June. In the control experiment, the cumulus boundary layer experienced transition from a condition that only forced cumulus exists (forced cumulus boundary layer) to a condition that active cumulus also exists (active cumulus boundary layer). The active cumulus onset was almost coincident with an abrupt drop of LFC. The LFC drop was attributed to a decrease of the local minimum value of saturated equivalent potential temperature at the bottom height of the inversion layer in addition to an increase of equivalent potential temperature near the land surface. After the active cumulus onset, the inversion height kept large increasing rate because the evaporation of cloud water cooled and moistened the inversion layer.

The systematic sensitivity experiments showed that the onset time became earlier with the larger initial water vapor, the smaller static stability, and the larger evaporative efficiency through change of time tendency of saturated equivalent potential temperature at bottom height of the inversion layer and equivalent potential temperature near the land surface. Since the active cumulus boundary layer showed large development rate, the earlier active cumulus onset led to higher inversion height and subsequent deeper moist layer. Even for the smaller Bowen ratio, which yielded shallower forced cumulus boundary layer, the inversion height after sunset did not change largely because the active cumulus onset became earlier. The active cumulus onset also affected the time tendency of total cloud fraction.

This study revealed the characteristics of the development of the dry convective boundary layer in the humid terrestrial area, the transition process from the forced to active cumulus

boundary layer and its impact on the atmospheric condition.

Contents

1 Introduction

The atmospheric boundary layer (ABL) appears as the result of surface forcings. Therefore, examination of the characteristics of the ABL can clarify the impacts of land surfaces on the atmosphere. In terrestrial areas, the ABL shows a strong diurnal change caused by land surface forcings, and a convective boundary layer (CBL) develops during daytime. Below the top of the CBL, thermal updrafts and interthermal downdrafts form vertical circulation, which transports heat, water vapor, momentum, and other quantities and creates a quasi-uniform layer. Such behavior of the CBL changes with the forcings of the underlying land surface (Stull, 1988; Garratt, 1992; Kaimal and Finnigan, 1994).

The height of the CBL top is a key parameter in describing the CBL. Tennekes (1973) presented a conceptual model for calculating the height of the CBL top from the sensible heat provided from the land surface. This model is called a "bulk" or "slab" model because the CBL is idealized as a layer of uniform air. Kaimal et al. (1976) showed a typical time series of the sensible heat flux and the height of the CBL top based on radiosonde observations. Continuous observation of the CBL top became possible with the development of remote sensors, such as wind profiler radar (WPR) (Ecklund et al., 1988; Angevine et al., 1994; Hashiguchi et al., 1995; Beyrich and Görsdorf, 1995; Grimsdell and Angevine, 1998; Cohn and Angevine, 2000). Yi et al. (2001) reported the seasonal change of diurnal variation of the surface flux and the CBL top estimated by WPR. The maximum CBL top coincided with the maximum surface sensible heat flux.

Vertical circulation plays a central role in the vertical transport in the CBL. The statistical characteristics of this circulation have been reported using data collected from aircraft observations (e.g., Young, 1988a,b). These thermal updrafts are driven by the buoyancy flux

in the CBL. In terrestrial areas, the buoyancy flux depends largely on the heat flux (e.g., Stull, 1988).

Extensive studies of the CBL over terrestrial areas have been conducted for the large, relatively dry plains of North America (e.g., Kaimal et al., 1976; Stull, 1988; Young, 1988a,b; Yi et al., 2001). In contrast to the wide, dry plains of North America, vast paddy fields cover large parts of eastern China, according to a land use map derived from satellite observations (cf. Loveland et al., 2000). Paddy fields supply large amounts of water vapor to the atmosphere (cf. Oue, 2005), but little research has been conducted on the CBL over such humid terrestrial areas.

The Huaihe River Basin of China has large areas of farmland on which double-cropping (wheat and rice) is practiced. In early summer, the vegetation changes from mature wheat fields to paddy fields. Several studies of deep convection were conducted in this region (e.g., Shinoda and Uyeda, 2002; Shusse et al., 2005; Shusse and Tsuboki, 2006) during the Global Energy and Water Experiment (GEWEX) Asian Monsoon Experiment (GAME)/Huaihe River Basin Experiment (HUBEX) (Zhao and Takeda, 1998). However, no study of CBL processes has been conducted in the area.

To investigate the CBL processes over the Huaihe River Basin, we conducted the Lower Atmosphere and Precipitation Study (LAPS) project as part of the Core Research for Evolutional Science and Technology (CREST) program, which implemented continuous monitoring and intensive observations in the area from August 2003 to January 2006. Tanaka et al. (2007) described the seasonal change of parameters with regard to the land surface (e.g., albedo, soil moisture), physical values near the surface (e.g., sensible heat flux, latent heat flux), and the height of the CBL top. The height of the CBL top was found to correlate with the sensible heat provided from the land surface, which was related to vegetation change;

the CBL top was low when paddy fields covered the land surface. The sensible heat flux was the primary controlling factor, as reported by previous studies of relatively dry terrestrial areas (e.g., Kaimal et al., 1976; Stull, 1988; Yi et al., 2001). However, although Tanaka et al. (2007) investigated the characteristics of the bulk structure of the CBL, the vertical circulation in the CBL has not been studied.

In addition to the dry CBL, the cumulus clouds are also important for the maintenance of the moisture field in this region (Shinoda et al., 2005). Cumulus clouds are closely tied to the CBL and affect the CBL processes of vertical transport of energy and water vapor. The behavior of cumulus clouds reflects surface forcings and atmospheric conditions, and cumulus clouds simultaneously transform atmospheric conditions through vertical transport of energy and water.

Fair-weather cumulus clouds are generated at the top of thermal updrafts penetrating into the inversion layer. Stull (1985) classified fair-weather cumulus clouds into the following three types. “ Forced cumulus ” reaches the lifting condensation level (LCL) but is lower than the level of free convection (LFC) and is therefore still defined by negative buoyancy. “ Active cumulus ” reaches the LFC and attains positive buoyancy. Finally, active cumulus that becomes disconnected from the mixed layer turns into “ passive cumulus. ”Among these three types, active cumulus transports mixed-layer air to higher levels.

Active cumulus clouds are an essential part of the trade wind cumulus boundary layer over the subtropical ocean (e.g., Siebesma and Cuijpers, 1995; Stevens et al., 2001; Siebesma et al., 2003). The trade wind cumulus boundary layer consists of a subcloud (mixed) layer, a cloud layer, and an inversion layer. The cloud layer is characterized by conditionally unstable stratification driven by positive-buoyancy active cumulus. Cumulus cloud reaching the LFC just above the LCL rises while being diluted by environmental air in the cloud layer. The

cumulus cloud that penetrates the inversion layer assumes negative buoyancy. Transport of cloud water is a major factor in the total water flux and enthalpy flux. The trade wind cumulus boundary layer is basically in a quasi-steady state due to continuous weak surface fluxes and dry, warm subsidence.

Over land, cumulus clouds develop with an underlying subcloud layer owing to the diurnal variation in large surface buoyancy flux. Wilde et al. (1985) investigated cumulus onset based on observations in Oklahoma in June 1983. They proposed an " LCL zone " to represent the range of height variations in the LCL calculated using values near the surface. The first cumulus was generated when the entrainment zone, which is nearly equal to the inversion layer, overlapped the LCL zone, i.e., when the highest thermal reached the lowest LCL. The total cloud fraction (cloudiness, cloud amount) increased as overlapping increased. Their method diagnoses cumulus onset reasonably well, because the core of thermal updraft rising from near the surface to the CBL top is only partly diluted (Crum et al., 1987). Zhu and Albrecht (2003) simulated a case of forced fair-weather cumulus clouds in the southern Great Plains of the U.S. on 6 July 1997. They developed a cumulus initiation diagnostic scheme based on the fact that the strongest thermal updraft results in the deepest penetration and generates the first cumulus. The supply of water vapor into the inversion layer was found to be important for the formation and development of the forced fair-weather cumulus clouds. Cloud water flux was less than one twentieth of water vapor flux. The development of forced cumulus was sensitive to the sensible and latent heat fluxes, the stability of the stratification, and the moisture difference across the CBL top; horizontal wind also had a minor influence.

Brown et al. (2002) showed the results of large eddy simulation based on idealization of a shallow cumulus case observed in the southern Great Plains on 21 June 1997. The shallow cumulus had positive buoyancy, and many aspects of the cumulus boundary layer,

except for the time evolution, were similar to the trade wind cumulus boundary layer over the subtropical ocean. The maximum height of the cumulus clouds increased rapidly under weak stratification. Khairoutdinov and Randall (2006) performed an idealized high-resolution simulation of shallow-to-deep cumulus transition over Amazonia on 23 February 1999. They focused on the initiation of deep cumulus convection and revealed that updrafts that lifted at the edge of the cold pool were necessary for the formation of deep cumulus circulation.

Although previous studies have examined the onset and development of cumulus clouds, little specific attention has been given to the onset of active cumulus. The cumulus boundary layer over land shows large diurnal variation due to large surface fluxes. However, it remains unclear which factors control the LFC and the transition process from forced to active cumulus boundary layers in the diurnal variation over land.

In this study, we conducted the observation at Showxian in the Huaihe River basin and performed high-resolution numerical simulations to clarify the development of the dry convective and cumulus boundary layers over a humid terrestrial area, the Huaihe River Basin in China. For the development of the dry CBL, we focused on the circulation and the vertical transport of heat and moisture in the convective boundary layer. For the development of the cumulus boundary layer, we focused particularly on the onset of active cumulus and its behavior under various surface flux and environmental conditions. As external factors, we adopted static stability, the initial amount of water vapor, and evaporative efficiency, which vary widely over humid terrestrial areas such as eastern China. This study uses the following notation for variables: $\phi = \overline{\phi} + \phi'$, where $\overline{\phi}$ and ϕ' indicate the mean (horizontally averaged) value and the perturbation from the mean value, respectively.

2 Study site and measurements

Under the LAPS project, continuous observations were performed using WPR, a Doppler sodar, a microwave radiometer, and a flux tower from August 2003 to January 2006 at Shouxian, Anhui Province, China (Fig. 1). The study site was located on a large plain along the Huaihe River. Being nearly flat and uniform, the site was suitable for a boundary layer experiment to study the effects of the land surface. In this study, we used the WPR and surface data obtained during an intensive observation period (IOP) in early summer of 2004 (IOP-2004: 24 May to 16 July). During this season, a surface transition is caused by the change in the crop in the double-cropping system. For a detailed description of the observations, see Tanaka et al. (2007).

Table 1 shows the operating specifications of the WPR. The WPR obtained data on the signal-to-noise ratio (SNR) and three-dimensional wind components. The frequency (1290 MHz) is suitable for observation of the lower atmosphere. The height and temporal resolution were 100 m and approximately 59 s, respectively. Surface fluxes were calculated from data obtained by flux sensors and radiation sensors set at a height of 32 m on the flux tower.

The SNR of the WPR is related to the structure parameter of the refractive index C_n^2, which depends on the turbulence intensity and the vertical gradient of the refractive index. In the lower atmosphere, C_n^2 mainly depends on the vertical gradient of water vapor (White et al., 1991). Therefore, the top of the CBL is detected as a large SNR because of the turbulence and the large gradient of water vapor between the humid boundary layer and dry free atmosphere (Angevine et al., 1994). In this study, we used the concept outlined above but also added a limit to the possible height range (Tanaka et al., 2007). The CBL top height was estimated within a variable range to avoid large SNRs near the surface or above

the actual CBL top. The variable range was set based on the assumption that the CBL top starts to develop just after sunrise at around 0600 local standard time (06 LST), reaches a maximum height between 12 and 16 LST, and does not change largely after 16 LST. This assumption was used to determine the variable range, and thus the actual CBL top did not have to follow the assumed development.

The CBL top was determined by the following procedure using the SNR data interpolated every 30 s (cf. Tanaka et al., 2007). First, the tentative maximum CBL top height on the day $h_{t,max}$ was determined. The height of the maximum SNR $h_{30s}(t)$ was selected for each time step. The tentative CBL top height at every hour $h_{t,1h}(t)$ was calculated as the median value of $h_{30s}(t)$ using a 4-h centered difference. $h_{t,max}$ was defined as the maximum $h_{t,1h}(t)$ between 12 and 16 LST. Second, based on $h_{t,max}$, the central value of the variable range at every hour $h_{c,1h}(t)$ was defined as follows. Between 12 and 16 LST, $h_{c,1h}(t)$ was given as the median of $h_{30s}(t)$ for 2 h between 0.5 $h_{t,max}$ and 1.2 $h_{t,max}$. Similarly, between 09 and 11 LST, $h_{c,1h}(t)$ was the median of $h_{30s}(t)$ for 2 h between 400 m and 1.2 $h_{c,1h}(t+1h)$; for example, 1.2 $h_{c,1h}$(12 LST) was used to determine $h_{c,1h}$(11 LST). The initial $h_{c,1h}$(06 LST) was 100 m. $h_{c,1h}$(07 LST) and $h_{c,1h}$(08 LST) were determined assuming linear development between 06 and 09 LST. $h_{c,1h}$(17 LST) and $h_{c,1h}$(18 LST) were equal to $h_{c,1h}$(16 LST). $h_{c,1h}(t)$ was linearly interpolated for each time step using a 30-s interval. Finally, the variable range was determined as $(1 \pm A)h_{c,1h}(t)$, where the constant A = 0.00 - 0.25 between 06 and 09 LST, 0.25 between 09 and 16 LST, and 0.25 - 0.30 between 16 and 18 LST. Within the height range, the height of the maximum SNR $h_{30s}(t)$ was selected again as the CBL top height z_i.

3 Numerical model and Experimental setup

The numerical model used for the simulations is the Cloud Resolving Storm Simulator (CReSS) (Tsuboki and Sakakibara, 2002) developed at Nagoya University. The CReSS is the compressible non-hydrostatic model for the high-resolution simulation. The CReSS has successfully simulated shallow clouds and boundary layer process (e.g., Liu et al., 2006; Maesaka et al., 2006; Nishikawa et al., 2009).

3.1 *Experimental setup for the simulations of dry convective boundary layer*

Table 2 shows the configuration for the numerical simulations of dry convective boundary layer. We applies a 1.5-order turbulence kinetic energy (TKE) closure as a sub-grid scale turbulent flux parameterization. Cloud microphysics parameterization are not used. The simulation spans a domain of 20 km $\times$ 20 km $\times$ 5888 m with a mesh of 200 $\times$ 200 $\times$ 120 points. The horizontal grid size is 100 m, which is sufficiently smaller than the horizontal scale of the thermal updraft estimated by the WPR observations. The vertical grid size is 30 m below 3000 m in height. Above 3000 m, vertical grid size is stretched and a sponge layer is adapted for absorbing gravity wave. The top boundary is rigid boundary condition and the lateral boundary is periodic boundary condition. The lower boundary is rigid boundary with surface layer parameterization of Louis et al. (1981). Soil temperature is predicted by one dimensional thermal diffusion. Land surface parameters were set as uniform (Table 3). These parameters were determined from the flux tower and manual observations to reproduce the observed surface fluxes from bare fields and paddy fields. The initial conditions were based on radiosonde data observed at 00 UTC (08 LST) at Fuyang (Fig. 1), which was the nearest sounding point. The simulations were executed for an integrated time of 12 hours

from 08 LST.

Figures 2 and 3 show the initial conditions for the dry-case and the wet-case, respectively. Potential temperature were stably stratified for dry convection. Humidity clearly differed between the two cases, with more humidity in the lower troposphere in the wet-case than in the dry-case. The mixing ratio of water vapor had a maximum near the land surface and was not mixed yet because the CBL was not active at 08 LST.

3.2 *Experimental setup for the simulations of cumulus boundary layer*

For the idealized simulations of cumulus boundary layer, several parameters are based on observational data obtained over paddy fields by the LAPS project (Tanaka et al., 2007) on 20 June 2004. On that day, observations at Shouxian suggested the occurrence of cumulus clouds. Figure 4 shows the SNR of the WPR and time series of the LCL and surface fluxes obtained at 32 m AGL. The CBL developed with the supply of small sensible and large latent heat fluxes. A large spike in the signal-to-noise ratio appeared above the LCL after approximately 12 LST. This spike was attributed to fluctuation in the refractive index of the atmosphere surrounding the cumulus clouds, as described by Kollias et al. (2001).

Table 4 shows the configuration for the present simulation. We applied a bulk method of warm rain processes as the microphysics parameterization and a 1.5-order turbulence kinetic energy closure scheme for the subgrid-scale turbulent flux parameterization. The simulation spanned a domain of 20 km $\times$ 20 km $\times$ 10 km with a mesh of 200 $\times$ 200 $\times$ 230 points. The horizontal grid size was 100 m, and the vertical grid size was 30 m below 6000 m height. Above 6000 m, the vertical grid size was stretched, and a sponge layer was adopted for absorbing gravity waves. The top boundary was a rigid boundary condition, the lateral boundary was a periodic boundary condition, and the lower boundary was a rigid boundary

with the surface-layer parameterization of Louis et al. (1981). Soil temperature was predicted by one-dimensional thermal diffusion. Table 5 shows the land surface parameters determined using observational data obtained at Shouxian. The external forcing was diurnal variation in shortwave radiation on 20 June at Shouxian. Interruption of shortwave radiation by clouds was diagnosed using the relationship to liquid water amount. The simulations were executed for a total integrated time of 14 h from 06 LST.

The idealized environment was given as the initial condition. Although the following design of the initial profile is almost the same as that used by Stevens (2007) for the cumulus boundary layer over ocean, this method can be used for the case of the CBL over land. Figure 5 shows the initial profile created for the control experiment and soundings at Fuyang at 08 LST (00 UTC). Pressure (solid line in Fig. 5c) was calculated on the basis of the hydrostatic equilibrium. The mixing ratio of water vapor q_v (solid line in Fig. 5b) exponentially decreases with height:

$$q_v(z) = q_0 \ \exp(-z/\lambda) \tag{1}$$

where q_0 is the surface water vapor mixing ratio and λ is a scale for height. For the control experiment, q_0 of 17 g kg^{-1} and λ of 2700 m were used. Virtual potential temperature was defined as

$$\theta_v \equiv \theta(1 + 0.61q_v - q_l) \tag{2}$$

where the liquid water mixing ratio q_l is zero at the initial condition. Virtual potential temperature (solid line in Fig. 5a) increases constantly with height, given as follows:

$$\theta_v(z) = \Gamma_v \ z + \theta_{v0} \tag{3}$$

where Γ_v is the vertical gradient of virtual potential temperature (static stability), and θ_{v0} is the virtual potential temperature at the surface. For the control experiment, Γ_v of 4.5 K

km^{-1} and θ_{v0} of 301.5 K were used. Because of the contribution of the water vapor given above, the vertical gradient of potential temperature was not constant. These parameters of the initial profile (lines in Fig. 5) were determined using the sounding profile at Fuyang at 08 LST (0000 UTC) (circles in Fig. 5). The values were the same as observations at the surface and similar to observations of the lower level.

The sensitivity experiments focused on three factors: initial amount of water vapor, static stability, and surface energy partition into sensible and latent heat fluxes. Figure 6 shows the components of the initial profiles for the sensitivity experiments. The amount of water vapor is controlled by surface water vapor q_0 in Eq. 1. Static stability is modified by the gradient of virtual potential temperature Γ_v in Eq. 3. These q_0 and Γ_v were the environmental parameters. In addition, surface evaporative efficiency β changes the surface energy partition. Table 6 gives the identification codes for the simulations and the parameters of the external factors. The control experiment, G45B25Q17 (bold italics), used (Γ_v, β, q_0) = (4.5, 0.25, 17). We first conducted the simulations including G45B25 (italics) using different initial water vapor (q_0 = 13, 14, 15, 16, 17 g kg^{-1}) as sensitivity experiments for the initial amount of water vapor. To check the behavior in the parameter spaces of Γ_v, β, and q_0, we next chose three points along the Γ_v axis (3.5, 4.5, 5.5 K km^{-1}), three points along the β axis (0.10, 0.25, 0.45), and four points along the q_0 axis (14, 15, 16, 17 g kg^{-1}). A total of 36 combinations (excluding G45B25Q13) were examined in the sensitivity experiments for static stability and surface energy partition.

4 Development of dry convective boundary layer

4.1 *The observation*

During the IOP-2004, land use changed from mature wheat fields to bare fields and then to paddy fields. Figure 7 shows the time series of the precipitation rate at the land surface, net radiation, and sensible and latent heat fluxes at 32 m AGL. The small net radiation on rainy days was caused by the interruption by clouds. There was an obvious difference between the first period, with mature wheat or bare fields, and the second period, with paddy fields. Although net radiation was little larger in the second period than in the first period, the sensible heat flux was much smaller. In the second period, much energy was partitioned to the latent heat flux because a large amount of water existed on the surface of the paddy fields. As a result, while the sensible heat flux was nearly equal to the latent heat flux in the first period, the latent heat flux was predominant in the second period.

Since distinct characteristics of the surface fluxes appeared in the first and second periods, two clear days were selected for detailed analysis. For these clear days, downward shortwave radiation showed a smooth curve with time, and the lack of clouds was confirmed by hemispherical photographs taken at the observation site. Two days, 31 May and 22 June 2004, were selected to represent the first and second periods and are referred to as the dry-case and wet-case, respectively.

The diurnal change of the surface fluxes and the CBL structure for the dry-case is shown in Fig. 8. In this case, the wheat had already been harvested, and the land surface was bare. Since the surface soil was easily heated because of its small heat capacity, the sensible heat flux became positive with the positive net radiation around 0630 LST (Fig. 8c). The sensible heat flux remained between 190 and 390 W m^{-2} from 09 to 16 LST, and the latent

heat flux stayed around 200 W m^{-2}. With the sensible heat flux, a deep CBL developed rapidly from early morning (Fig. 8a). The height of the CBL top began to increase at 0730 LST, reaching 1600 m at 10 LST, 1900 m at 12 LST, and a maximum height of 2250 m at about 14 LST. Updraft and downdraft occurred in the entire CBL until about 1630 LST, thus forming circulation (Fig. 8b). The maximum value of the thermal updraft was about 3 m s^{-1}. The horizontal scale of the thermal updrafts was about 720 - 3600 m, assuming the drift with a 5 m s^{-1} time-averaged horizontal wind speed. The horizontal scale of the circulation (distance between updrafts) was at least 3 km based on the same assumption. After around 1630 LST, the average thermal top lowered gradually, although the thermals reaching high altitude were still present.

For the wet-case, a shallow CBL developed slowly from late morning (Fig. 9). Although the net radiation became positive at 06 LST, the sensible heat flux remained nearly zero until 10 LST (Fig. 9c). Between 12 and 13 LST, the net radiation reached its maximum value of 700 W m^{-2}, while the sensible heat flux was only about 100 W m^{-2}. In contrast to the sensible heat flux, the latent heat flux maintained large values between 320 and 560 W m^{-2} from 10 to 16 LST. There were large amounts of water on the surface of the paddy fields, and a large amount of energy was consumed in evapotranspiration. The CBL started to develop at 10 LST, 2.5 hours later than in the dry-case, and gradually increased its top height (Fig. 9a). The height of the CBL top was 700 m at 12 LST, 1100 m at 14 LST, and stopped developing at about 1740 LST, when the sensible heat flux neared zero. The maximum height of the CBL top was about 1400 m. Repetition of weak vertical motion was seen in the CBL (Fig. 9b). The maximum value of the thermal updraft was about 1.5 m s^{-1}, the horizontal scale of the thermal updrafts was approximately 720 - 3600 m, and the horizontal scale of the circulation was at least 1.3 km. The height of thermal top tended to

be low after around 1630 LST.

Table 7 summarizes the results of the observations. The characteristics of the surface fluxes, the development of the CBL, and the structure of the circulation in the CBL in each case are presented.

4.2 *The simulation*

We conducted a numerical LES to clarify the three-dimensional structure of the CBL, including the temperature and humidity, and to evaluate the vertical fluxes of heat, moisture, and buoyancy.

Figure 10 presents time-height sections of potential temperature (a) and vertical velocity (b) with the mixing ratio of water vapor [contours in (a, b)] at the center of the model domain and time series of the surface fluxes (c) for the dry-case. The large vertical gradient of water vapor [the dense contours in (a, b)] corresponds to the top of the CBL. The sensible heat flux was slightly larger than the latent heat flux (c), and a deep CBL developed rapidly (a, b). The maximum height of the CBL top was about 2400 m, which is only 150 m higher than that of the observed CBL top shown in Fig. 8. The potential temperature (a) did not change with time above the CBL top and, therefore, the free atmosphere remained stably stratified. In the CBL, the potential temperature was uniform with height because of the mixing by updrafts and downdrafts (b) and gradually increased with time.

For the wet-case (Fig. 11), a shallow CBL developed slowly (a, b) as a result of the small sensible heat flux and large latent heat flux from the land surface (c). The maximum height of the CBL top was about 1300 m, which is only 100 m lower than that of the observed CBL top shown in Fig. 9. The potential temperature (a) was stratified above the CBL top and was also uniform in the CBL, as in the dry-case. The large water vapor in the CBL (a, b)

resulted not only from the initial condition, but also from the supply from paddy fields. The gradient of water vapor at the CBL top was larger than that for the dry-case.

Figure 12 shows the vertical cross section of vertical velocity (shading) and potential temperature (contours) at 14 LST, when the vertical circulation was active, for the dry-case (a) and the wet-case (b). The CBL top appears as the large vertical gradient of the potential temperature around 2100 m for the dry-case and around 900 m for the wet-case. In the CBL, the gradient of potential temperature was small, and thermal updrafts and interthermal downdrafts were active. The CBL top was high over the updraft region and low over the downdraft region. The CBL top height fluctuated in a range of about 300 m for both cases. Weak vertical motion of gravity wave extended above the CBL top (cf. Young et al., 2002), which is also represented in the time-height sections (Figs. 10 and 11). This circulation was similar to the WPR results when the circulation was assumed to drift with the mean horizontal wind.

Figure 13 shows the horizontal distribution of vertical velocity, the fluctuations of potential temperature, and the mixing ratio of water vapor at the middle level of the CBL ($z/z_i \sim 0.5$, where z_i is the height of the CBL top) at 14 LST for the dry-case. The fluctuations of potential temperature and water vapor had a similar pattern to that of the vertical velocity (Figs. 13a - 13c). According to Figs. 13d - 13f, which show close-up views of the black squares in Figs. 13a - 13c, the potential temperature and mixing ratio of water vapor had large (small) fluctuations in areas of updrafts (downdrafts). Vertical velocity correlated positively with the fluctuation of potential temperature and water vapor. This means that the circulation transported heat and water vapor. For the wet-case (Fig. 14), the potential temperature and mixing ratio of water vapor had smaller horizontal scale structures. Vertical velocity also had small horizontal scale for the updraft and circulation. In areas of updraft,

the fluctuations of water vapor showed positive values similar to those of the dry-case; however, the fluctuations of potential temperature tended to be negative. The correlation of vertical velocity and potential temperature was weaker than that vertical velocity and water vapor and was sometimes negative.

The vertical fluxes of heat, moisture, and buoyancy were calculated from the fluctuations of temperature and water vapor. For compatibility with buoyancy flux, we show the heat flux $\overline{w'\theta'}$ and moisture flux $\overline{w'q'_v}$ in and above the CBL. These are substitutes for the sensible heat flux $\rho C_p \overline{w'\theta'}$ and latent heat flux $\rho L_v \overline{w'q'_v}$, which are useful for examining energy partition at surface; here, ρ is density, C_p is specific heat at constant pressure, and L_v is the latent heat of vaporization. Figures 15 and 16 show the vertical fluxes averaged over the entire model domain at 14 LST. For both cases, the subgrid-scale fluxes of heat and moisture (dotted lines in Figs. 15a, 15b, 16a, and 16b) reached maximum values near the land surface and became zero at heights where the resolved fluxes (solid lines in the same figures) had become large. The subgrid-scale fluxes existed only near the surface and compensated for the resolved fluxes. The total flux is the sum of the subgrid-scale and resolved fluxes. The resolved heat fluxes (solid lines in Figs. 15a and 16a) reached maximum values (0.226 K m s^{-1} for the dry-case and 0.041 K m s^{-1} for the wet-case) near the land surface and constantly decreased with height. This indicates homogeneous heating of the entire CBL by the circulation. The resolved heat fluxes showing negative values near the CBL top indicate entrainment from the free atmosphere, which had a high potential temperature. The resolved moisture fluxes (solid lines in Figs. 15b and 16b) were nearly constant (about 0.10 g kg^{-1} m s^{-1} for the dry-case and 0.17 g kg^{-1} m s^{-1} for the wet-case) with height in the CBL and became zero near the CBL top. Thus, the circulation moisturized the atmosphere only near the CBL top.

The buoyancy associated with the buoyancy flux drives the thermal updrafts. The buoy-

ancy flux $\overline{w'\theta'_v}$ can be written as

$$\overline{w'\theta'_v} = 0.61\overline{\theta}\ \overline{w'q'_v} + \overline{w'\theta'}(1 + 0.61\overline{q_v}) + 0.61\overline{w'q'_v\theta'} \tag{4}$$

$$\simeq 0.61\overline{\theta}\ \overline{w'q'_v} + \overline{w'\theta'}(1 + 0.61\overline{q_v}) \tag{5}$$

The triple correlation $\overline{w'q'_v\theta'}$ was negligible because it was much smaller than other terms (Stull, 1988). As shown above, the buoyancy flux $\overline{w'\theta'_v}$ consists of the contribution of moisture $0.61\overline{\theta}\ \overline{w'q'_v}$ and that of heat $\overline{w'\theta'}(1 + 0.61\overline{q_v}) \simeq \overline{w'\theta'}$. The moisture contribution is due to the fact that water vapor is less dense than dry air. For the dry-case (Fig. 15c), the contribution of heat (0.226 K m s^{-1} at maximum) was one order larger than that of moisture (0.018 K m s^{-1}). As a result, the vertical profile of the buoyancy flux was nearly equal to that of the contribution of heat. Namely, for the case in which the sensible heat flux at the surface was nearly equal to the latent heat flux, almost all of the buoyancy depended on the heat provided from the land surface. For the wet-case (Fig. 16c), the contribution of moisture in the CBL was nearly constant at about 0.032 K m s^{-1}, although that for the dry-case was constant at about 0.018 K m s^{-1}, showing that the contribution of moisture was 1.7 times larger than for the dry-case. The contribution of heat was a maximum value of 1/5 (0.041 K m s^{-1}) that of the dry-case (0.226 K m s^{-1}). As a consequence, the contributions of heat and moisture were of the same order. In other words, the difference in the density, which was caused not only by heat but also by water vapor, yielded the buoyancy. For the case in which the latent heat was predominant at the land surface, the water vapor was a considerable source of buoyancy.

The initial profiles of potential temperature and water vapor were modified by the CBL process. Figure 17 shows the vertical profiles of the simulation and the sounding data for Fuyang at 08 LST (00 UTC; initial condition) and 20 LST (12 UTC; end of the simulation)

in the dry-case. The initial conditions of the simulations (broken lines) were given by the sounding at 08 LST at Fuyang (solid squares); thus, the two profiles are the same. After integration for 12 hours, the simulated profiles at 20 LST (solid lines) had been modified by the vertical flux including the surface flux and the entrainment flux. However, the simulated profiles did not completely correspond to the soundings (open circles). The simulation shows well-mixed profiles while the soundings had a small vertical gradient. For the wet-case (Fig. 18), the water vapor in the CBL increased largely as a result of the large water vapor supply from the land surface. The sounding profile showed a larger vertical gradient.

5 Development of cumulus boundary layer

5.1 *The control experiment*

The development of cumulus clouds in the control experiment is presented in Fig. 20, which shows time series of the total cloud fraction (a) and time-height sections of the cloud fraction with time series of the LCL, LFC, and level of neutral buoyancy (LNB; also called the limit of convection) (b). The total cloud fraction represents the ratio of the column area in which cloud water exceeded 0.01 g kg^{-1}. The LCL, LFC, and LNB were derived from horizontal mean values at 45 m height. The total cloud fraction began to increase at 0920 LST, and the cloud fraction exceeded the value of 0.01 at 700 m height at 10 LST. The cloud layer deepened until around 17 LST. The cloud base height increased until mid-afternoon with an increase in the LCL. While the top and bottom of the cloud layer changed smoothly, the LFC discontinuously decreased from 2700 m at 1210 LST to 1100 m at 1220 LST. The LNB also decreased largely but then increased again at 1440 LST. Until around 12 LST, the total cloud fraction increased gradually and showed a single peak near the cloud base height until the abrupt drop in the LFC. After the LFC drop, the total cloud fraction maintained a nearly constant value of 0.25, and the cloud fraction tended to have an additional peak near the top of the cloud layer.

Figure 21 shows time-height sections of the variance of vertical velocity with mean virtual potential temperature (a), the mean relative humidity with the mixing ratio of water vapor (b), and the mean surface flux time series (c). The surface fluxes had a feature common to paddy areas; namely, the peak time of large latent heat flux was delayed relative to that of small sensible heat flux. The inversion height (broken line in Fig. 21a) is defined as the height at which the gradient of virtual potential temperature attains its maximum value.

The inversion height was close to the top of the cloud layer and increased until sunset. In the subcloud layer, dry convection seen as large variance of vertical velocity changed with the diurnal variation in surface flux. Until the LFC drop just after 12 LST, virtual potential temperature and water vapor had well-mixed profiles, and relative humidity increased with height below the inversion height. While the virtual potential temperature increased with time, the water vapor gradually decreased. In the cloud layer after the LFC drop, virtual potential temperature and water vapor had vertical gradients, and relative humidity had a nearly constant value of 85%.

Next we examined the cumulus and CBL structures before and after the LFC drop. Figure 22 shows vertical cross-sections of cumulus boundary layer in a plane adjacent to the center of the model domain at 11 and 13 LST. At 11 LST, cumulus clouds (thick lines) were generated by the strong updraft penetrating into the inversion. The updrafts involved larger amounts of water vapor than the surrounding atmosphere, which was favorable for the formation of higher relative humidity, a lower LCL, and subsequent condensation. Although water vapor condensed and released latent heat around the top of the updraft, virtual potential temperature was still lower in the cumulus clouds than in the surrounding atmosphere. Therefore, these clouds were identified as forced cumulus clouds with negative buoyancy. At 13 LST, cumulus clouds were generated at the top of the updraft, the same as at 11 LST. However, in contrast to the case of the cumulus clouds at 11 LST, virtual potential temperature in the most vigorous cloud was higher than that of the surrounding atmosphere, and therefore this cloud attained positive buoyancy. Active cumulus cloud was also present in addition to the forced cumulus clouds. The cloudy air rose with the heat, water vapor, and cloud water.

The CBL develops as a result of vertical flux induced by the updrafts and cumulus clouds

mentioned above. Figure 23 shows profiles of the cloud fraction and resolved vertical flux at 11 and 13 LST. The active cloud fraction (broken line in Figs. 23a and 23e) is the fraction of cloud elements with positive buoyancy, often called the core fraction (e.g., Brown et al., 2002). The active cloud fraction was zero at 11 LST (Fig. 23a), indicating that all cumulus clouds were forced cumuli. However, at 13 LST (Fig. 23e) the active cloud fraction accounted for about two third of the cloud fraction near the cloud base height.

The vertical fluxes at 11 LST are shown in Figs. 23b, 23c, and 23d. Total water flux $\overline{w'q'_t}$ is written as

$$\overline{w'q'_t} = \overline{w'q'_v} + \overline{w'q'_l} \tag{6}$$

which is the sum of the water vapor flux $\overline{w'q'_v}$ and liquid water flux $\overline{w'q'_l}$. Because the precipitation fluxes are nearly zero in the present case, the liquid water flux equals the cloud water flux ($\overline{w'q'_l} = \overline{w'q'_c}$). At 11 LST, the cloud water flux was less than one tenth of the water vapor flux, and almost all water was transported as water vapor. The water vapor flux showed divergence in the subcloud layer and convergence in the inversion layer. Thus, in addition to water vapor flux in the surface layer, water vapor in the subcloud layer also contributed to moistening the inversion layer. The liquid water potential temperature is written as

$$\theta_l = \theta \exp\left(\frac{-q_l L_v}{c_{pd} T}\right) \tag{7}$$

where L_v is the latent heat of vaporization of water and c_{pd} is the specific heat at constant pressure. Liquid water potential temperature is the potential temperature at which all liquid water evaporates and is conserved under moist adiabatic transformations (Emanuel, 1994). Its mean value was almost equal to potential temperature in the present case. Liquid water

potential temperature flux, which is equivalent to the flux of enthalpy, can be written as

$$\overline{w'\theta'_l} \simeq \overline{w'\theta'} - \left(\frac{\overline{\theta}}{\overline{T}}\right)\frac{L_v}{c_p}\overline{w'q'_l} \tag{8}$$

which is the sum of the transport in the form of potential temperature $\overline{w'\theta'}$ and that of liquid water $\overline{w'q'_l}$ (cf. Siebesma et al., 2003). Because liquid water is able to evaporate, taking energy from the surrounding air, upward liquid water flux is equivalent to downward enthalpy flux. At 11 LST, the contribution of liquid water occupied half of the liquid water potential temperature flux in the inversion layer. This means that forced cumulus enhanced cooling in the inversion layer and contributed to deepening the CBL. Virtual potential temperature flux called buoyancy flux is written as

$$\overline{w'\theta'_v} \simeq 0.61\ \overline{\theta}\ \overline{w'q'_v} - \overline{\theta}\ \overline{w'q'_l} + \overline{w'\theta'}\ (1 + 0.61\ \overline{q_v} - \overline{q_l}) \tag{9}$$

which is the sum of the contributions of potential temperature flux $\overline{w'\theta'}\ (1 + 0.61\ \overline{q_v} - \overline{q_l}) \simeq \overline{w'\theta'}$, water vapor flux $0.61\ \overline{\theta}\ \overline{w'q'_v}$, and liquid water flux $\overline{\theta}\ \overline{w'q'_l}$. Water vapor contributes to buoyancy because it is less dense than dry air, and the contribution of liquid water is due to the weight of liquid water (Stull, 1988). At 11 LST, the buoyancy flux consisted only of the contributions of potential temperature and water vapor fluxes. The buoyancy flux was similar in shape to the dry CBL except for the slight positive value around the CBL top. In summary, at 11 LST, the forced cumulus only modulated the dry CBL with regard to water and buoyancy fluxes. However, the contribution of the forced cumulus to the development of the CBL was not negligible in terms of the liquid water potential temperature flux.

Whereas only forced cumulus clouds existed at 11 LST, active cumulus clouds were also present at 13 LST (Figs. 23e - 23h). Upward water transport as a form of cloud water flux increased in the cloud layer (1100 - 1450 m) and decreased in the inversion layer above. The cloud water flux made a large contribution to the total water flux in the cloud and

inversion layers. The potential temperature flux increased from the bottom of the cloud layer to the middle of the inversion layer because of the heat caused by condensation. In contrast to the potential temperature flux, liquid water flux produced downward liquid water potential temperature flux. The liquid water potential temperature flux showed convergence (heating) in the subcloud and cloud layers and divergence (cooling) in the inversion layer. The buoyancy flux increased with height in the cloud layer because the increased contribution of potential temperature flux merged with that of water vapor flux extending from the subcloud layer. The negative contribution of liquid water was not negligible but was smaller than the contributions of potential temperature and water vapor. In summary, at 13 LST, active cumulus having positive buoyancy due to condensation heating played a considerable role as carriers of heat and water. These clouds heated the cloud layer and cooled and moistened the inversion layer.

The reason for the large decrease in the LFC is illustrated in Fig. 24, which shows the time variation of profiles of mean equivalent potential temperature and saturated equivalent potential temperature. Equivalent potential temperature and saturated equivalent potential temperature are written as

$$\theta_e \ = \theta_d \ \exp\left(\frac{q_v L_v}{c_{pd} T_{LCL}}\right) \tag{10}$$

and

$$\theta_e^* \ = \theta_d \ \exp\left[\frac{q_{vs}(T) L_v}{c_{pd} T}\right], \tag{11}$$

respectively, where T_{LCL} is temperature at the LCL, q_{vs} is saturation water vapor, and $\theta_d = T[p_0/(p-e)]^{R_d/c_{pd}}$ is dry potential temperature. Equivalent potential temperature (solid line) had a well-mixed profile in the subcloud (mixed) layer and increased slowly with time. However, a local minimum of saturated equivalent potential temperature (broken line)

appeared at the height of the bottom of the inversion layer at 09 LST. The value of the local minimum decreased with the evolution of the dry convective and forced cumulus boundary layers (from 354.5 K at 09 LST to 351.7 K at 11 LST). As a result, the LFC decreased from 2850 m to 1170 m between 11 and 13 LST. The local minimum value of saturated equivalent potential temperature was a key element in the time variation in the LFC (Fig. 20). The LNB also decreased largely and then increased again until 15 LST. Note that the local minimum of saturated equivalent potential temperature was located at the bottom of the inversion layer. The value of the local minimum decreased with the increase in the inversion height.

Figure 25 shows a histogram of equivalent potential temperature with its mean value and mean saturated equivalent potential temperature at the bottom of the inversion layer (a: 1125 m), middle (b: 645 m), and lower subcloud layer (c: 195 m) and near the surface (d: 45 m) at 1220 LST just after the LFC drop. Naturally, the mean equivalent potential temperature at 45 m height was slightly higher than the mean saturated equivalent potential temperature at 1125 m height. At the lower subcloud layer (195 m), updraft (white line) involved air of high equivalent potential temperature reflecting the air properties near the surface (45 m). The updraft with high equivalent potential temperature extended through the middle of the subcloud layer (645 m) and was included in cloud (black line) at the bottom of the inversion layer (1125 m). At this height, the larger edge of the distribution reached the local minimum value of mean saturated equivalent potential temperature. Hence, active cumulus began to be generated at around the time of the LFC drop. The LFC drop corresponded to the onset of the active cumulus.

5.2 *The sensitivity experiments for the initial amount of water vapor*

This subsection shows the results of the five sensitivity experiments for the initial amounts of water vapor created by q_0 = 13 to 17 g kg^{-1}. In the control experiment, q_0 of 17 g kg^{-1} was used.

Figure 26 shows time series of mean surface fluxes in the sensitivity experiments. Variability among the simulations was small, and the land surface supplied similar amounts of heat and water vapor to the atmosphere. As the initial water vapor decreased, the net radiation increased from late morning to early evening, because downward shortwave radiation increased due to the lack of clouds. The latent heat flux also increased because of the increase in net radiation and the difference between surface saturation water vapor and water vapor at the bottom of the atmosphere. Sensible heat flux values were almost the same.

Figure 27 presents time series of inversion height with the onset time of forced cumulus (black symbols) and active cumulus (white symbols). The onset time of forced cumulus was delayed along with the decrease in initial water vapor. The inversion height was slightly higher in the case that yielded the forced cumulus earlier. The onset time of active cumulus was also delayed, and onset did not occur in the simulations for q_0 = 13 and 14 g kg^{-1}. For a period in which active cumulus clouds were also present, the inversion height had a larger rate of increase compared to the case of no active cumulus. As a consequence, earlier active cumulus onset led to higher inversion height.

Figure 28 presents time series of mean equivalent potential temperature near the surface ($\overline{\theta_e(z_s)}$) and mean saturated potential temperature at the height of the minimum of liquid water potential temperature flux ($\overline{\theta_e^*(z_{ib})}$). Because z_{ib} generally corresponds to the bottom of the inversion layer for dry convective, forced cumulus, and active cumulus boundary layers,

$\overline{\theta_e^*(z_{ib})}$ is equivalent to the local minimum value of mean saturated potential temperature shown in Fig. 24. The intersection points of the gray and white lines correspond to the active cumulus onset, as in Fig. 27. As mentioned above, active cumulus onset did not occur in the simulations for $q_0 = 13$ and 14 g kg^{-1}. Because θ_e is a function of water vapor, the values of $\overline{\theta_e(z_s)}$ at 09 LST differed among the simulations. The values of $\overline{\theta_e(z_s)}$ increased with time because of sensible heat and water vapor supplied from the surface to the subcloud layer. The rate of increase was large in the morning and small in late afternoon, depending on the balance between the supply from the surface and the depth of the boundary layer (the lower heating efficiency for the deeper layer). In particular, $\overline{\theta_e(z_s)}$ stopped increasing at around the time of active cumulus onset, which was apparent in the simulation for $q_0 = 17$ g kg^{-1}. The values of $\overline{\theta_e^*(z_{ib})}$ also differed slightly at 09 LST because of the initial difference in θ (we set different q_v with the same θ_v profile). The values of $\overline{\theta_e^*(z_{ib})}$ decreased rapidly with time, accompanied with the increase in the inversion height as mentioned in regard to Fig. 24. The simulation initialized with more water vapor showed a slightly larger rate of decrease even before active cumulus onset because the earlier forced cumulus onset made the inversion higher.

The profiles of virtual potential temperature and the water vapor mixing ratio changed between morning and evening as a result of the formation of the cumulus boundary layer. Figure 29 shows profiles of the virtual potential temperature and water vapor mixing ratio at 06 LST (initial condition) and 19 LST, and their differences between those times. Naturally, the profiles of virtual potential temperature overlapped at 06 LST. At 19 LST, the residual subcloud layer, cloud layer, and inversion layer were present for the simulations with $q_0 = 15$, 16, and 17 g kg^{-1}, which produced the active cumulus clouds. Among these simulations, the thickness of cloud layer changed depending on the amount of initial water vapor. The

cloud layer did not form in the simulations with q_0 = 13 and 14 g kg^{-1} because active cumulus onset did not occur. All simulations showed similar difference in virtual potential temperature in the subcloud layer. The virtual potential temperature increased more at the lower level and decreased in the cloud and inversion layers as the cloud layer thickness increased. However, the structure of water vapor also corresponded to the subcloud, cloud, and inversion layers. Water vapor was trapped in the subcloud layer in the cases without active cumulus. For the cases with active cumulus, greater amounts of water vapor were distributed in the higher level.

5.3 *The sensitivity experiments for the static stability and surface energy partition*

This subsection presents the results of the sensitivity experiments for the static stability (Γ_v = 3.5, 4.5, 5.5 K km^{-1}) and surface evaporative efficiency (β = 0.10, 0.25, 0.40) in addition to the initial amount of water vapor (q_0 = 14, 15, 16, 17 g kg^{-1}). The four simulations in the previous subsection are included as the set of (β, Γ_v) = (0.25, 4.5).

Figure 30 shows time series of latent and sensible heat fluxes in the 36 simulations classified into three groups by surface evaporative efficiency. The surface energy partition was mainly controlled by evaporative efficiency. Greater evaporative efficiency resulted in larger latent and smaller sensible heat fluxes (i.e., smaller Bowen ratios). The small variability in the latent heat flux is attributed to the difference in initial water vapor, as shown in Fig. 26.

Figure 31 presents time series of inversion height for the sensitivity experiments. Each panel shows the results of the four simulations using different initial amounts of water vapor and the same evaporative efficiency and static stability. The center panel (e) gives the results

of the four simulations shown in the previous section. Active cumulus clouds are present after approximately the active cumulus onset time (white symbols). The features for initial water vapor shown in the previous section are common in all the groups; namely, greater water vapor resulted in earlier onset timing and higher inversion height. With the decrease in static stability (top to bottom panels), active cumulus onset occurred earlier and there was a greater rate of increase in the inversion height for periods both before and after the active cumulus onset. As a result, the inversion became higher in the whole period. With the increase in evaporative efficiency (left to right panels), the onset time became earlier while the growth rate became smaller before onset. Small sensible heat flux led to a shallow CBL, even though the forced cumulus supported CBL growth. However, the differences in the inversion height after sunset did not change largely because the active cumulus onset time became earlier. For the simulations with $q_0 = 17$ g kg^{-1} and $\Gamma_v = 3.5$ K m s^{-1}, deep precipitating clouds (Khairoutdinov and Randall, 2006) appeared between 1530 and 1600 LST. Because this study does not focus on the evolution to deep precipitating clouds, results after 1530 LST in these cases are excluded from the following analysis.

Figure 32 presents time series of mean equivalent potential temperature near the surface $\overline{\theta_e(z_s)}$ and mean saturated equivalent potential temperature at the bottom of the inversion layer $\overline{\theta_e^*(z_{ib})}$ for the sensitivity simulations. The values of $\overline{\theta_e^*(z_{ib})}$ are are based on the same method as those in Fig. 28. With the decrease in static stability (top to bottom panels), the values of $\overline{\theta_e^*(z_{ib})}$ significantly decreased because of the larger rate of increase in z_{ib} (Fig. 31). The increase in $\overline{\theta_e(z_s)}$ was suppressed because of the limited amount of water vapor distributed to the deep boundary layer (i.e., water vapor flux divergence should be large in the subcloud layer). Although the increase in $\overline{\theta_e(z_s)}$ became smaller, the larger decrease in $\overline{\theta_e^*(z_{ib})}$ made the onset time earlier. With the increase in surface evaporative efficiency (left

to right panels), $\overline{\theta_e(z_s)}$ increased because of greater water vapor supply to the thinner layer. The change in $\overline{\theta_e^*(z_{ib})}$ was small. The earlier active cumulus onset was mainly caused by larger $\overline{\theta_e(z_s)}$.

Figure 33 shows time series of the total cloud fraction. The forced cumulus onset and evolution became earlier with the decrease in static stability (top to bottom panels) and the increase in surface evaporative efficiency (left to right panels). The active cumulus onset changed the time tendency of the total cloud fraction. The total cloud fraction increased until the time of active cumulus onset and stopped increasing at a nearly constant value or began to decrease after the active cumulus onset. As the surface flux decreased in late afternoon, the total cloud fraction decreased, except for when precipitating clouds appeared.

Figure 34 shows the water vapor mixing ratios at 19 LST for the sensitivity simulations. Figure 35 shows the difference in water vapor mixing ratios between 06 LST and 19 LST for the sensitivity simulations. Water vapor was distributed to higher levels in the cases involving the active cumulus and was trapped in the subcloud layer in the cases without active cumulus onset. With the decrease in static stability (top to bottom panels), the height range in which water vapor increased extended higher, because both the forced and active cumulus boundary layers developed deeper. With the increase in surface evaporative efficiency (left to right panels), water vapor increased in the lower level. This feature was attributed to greater water vapor supply and small water vapor flux divergence in the subcloud layer. Although the difference in the inversion height was small, the amount of water vapor increase at certain levels depended on the thickness of each layer.

6 Discussion

6.1 *Reproducibility of the simulations*

For the simulations of the dry CBL, the surface flux, the development of the CBL, and the circulation in the CBL agreed well with the observations, although there were some differences. The starting time of the simulated development of the CBL was 1.5 hours later than the observed time for the dry-case (Figs. 8 and 10). The delayed development of the CBL was due to the use of 08 LST as the initial time. Sounding data for the initial condition were only available at 08 LST, but the observed sensible heat flux showed a positive value after 0630 LST, and the observed CBL had already started to develop at 0730 LST (Fig. 8), much earlier than the initial time of 08 LST used for the simulation.

For the wet-case, the CBL started to develop 1 hour earlier than the observed time (Figs. 9 and 11). The earlier development of the CBL appears to have been caused by the complex land surface process of paddy fields. The simulation did not reproduce the observed late rise of the sensible heat flux. The layer of shallow water that covers the surface of flooded paddy fields has a large heat capacity. Because the surface temperature of such water bodies increases slowly, the rise of the sensible heat flux was delayed. The slow development of the observed sensible heat flux (Fig. 9c) was not reproduced by the simulation (Fig. 11c) using the simple bulk model (Louis et al., 1981). For further improvement of the simulation of the CBL over paddy fields, a land surface scheme that considers the water heat storage of paddy fields (e.g., Kim et al., 2001; Tanaka, 2004) is required.

The simulated profiles also did not completely correspond to the soundings. For the dry-case (Fig. 17), the simulated profiles showed a well-mixed layer and sharp inversion, while the sounding profiles showed a small gradient. The difference was larger for the wet-case

(Fig. 18) than for the dry-case. The difference can be explained by active entrainment. The simulated entrainment was apparently smaller than the entrainment suggested by the sounding. The vertical gradients of the observed profiles in the wet-case are possibly caused by large entrainment flux induced by shallow cumulus clouds. The sounding data imply the appearance of shallow cumulus clouds around Fuyang and, however, the cumulus were not found at Shouxian. On the otherhand, the simulated CBL was clear (i.e. no cloud) and, however, had abundant water vapor. In this humid condition, a small difference of surface flux exerts an influence on the generation of the cumulus. Another possiblity is influence of the descent of the thermal top height (mixing height) in late afternoon. The descent of the mixing height were clearer in observed cases (Figs. 8 and 9) than in the simulations (Figs. 10 and 11). A fine-grided simulation dealing with large-scale subsidence should be necessary for precise evaluation of the influence.

For the cumulus boundary layer, we conducted the simulation using the idealized profile. However, the simulated feature basically followed that of the observed cumulus boundary layer in terms of the time variation of the LCL and cloud top height.

6.2 *The characteristics of the dry CBL over a humid terrestrial area*

The characteristics of the surface fluxes, the development of the CBL, and the structure of the circulation clearly differed between the wet-case and the dry-case (Table 7). The sensible heat flux was smaller for the wet-case than for the dry-case because a large amount of energy was partitioned to latent heat flux. The height of the CBL top mainly depends on surface sensible heat flux (cf. Tennekes, 1973). Therefore, the CBL top for the wet-case became lower than that for the dry-case. The slight sensible and huge latent heat fluxes and the slow development of the low CBL top, due to the presence of surface water, should be a feature

of the CBL over humid terrestrial areas. Tanaka et al. (2007) also confirmed the presence of a low CBL top over paddy fields; that study showed seasonal variation in surface conditions and the CBL top height for a period including the IOP-2004.

The amount of surface flux also affects the circulation in the CBL. A forced air mass that is positively buoyant ascends and forms thermal updrafts. The thermal updraft is weaker in the wet-case than in the dry-case, so the thermal updraft has less buoyancy in the wet-case than in the dry-case.

The source of the buoyancy was examined using the simulation results. For the dry-case, the sensible heat flux from bare fields was slightly larger than the latent heat flux (Fig. 10), and the buoyancy flux largely depended on the heat flux in the CBL (Fig. 15). The relationship between the buoyancy flux and the surface heat flux was similar to that reported for relatively dry terrestrial areas (Stull, 1988). Under these condition, the sensible heat flux from the land surface was much more important than the latent heat flux in the development of the CBL (Tennekes, 1973; Kaimal et al., 1976; Stull, 1988; Yi et al., 2001).

On the other hand, for the wet-case, paddy fields provided small sensible and large latent heat fluxes to the CBL (Fig. 11), and the contribution of moisture to the buoyancy flux was as large as that of heat due to the large supply of water vapor from the paddy fields (Fig. 16). This condition is particular to humid terrestrial areas and differs from that in the dry-case in the present study and the relatively dry terrestrial sites of previous studies. In humid terrestrial areas, where the latent heat flux is much larger than the sensible heat flux, the large amount of water vapor is as important as heat in the development of the CBL.

In addition, the contribution of heat decreases with time. Figure 19 shows the time variation of the buoyancy flux and the contributions of heat and moisture in the wet-case. Near the surface, the contribution of heat was larger than that of moisture at 12 LST, nearly

equal to it at 14 LST, and below zero, except near the surface at 16 LST. The negative value of the heat flux was caused by the entrainment of air from the free atmosphere having high potential temperature. The positive value of the buoyancy flux was yielded only by the contribution of moisture at 16 LST.

The negative value of the heat flux and the contribution of moisture to most of the buoyancy flux have also been found in CBL processes over the tropical and subtropical oceans (e.g., Nicholls and LeMone, 1980). However, the vertical fluxes in the oceanic CBL were one order smaller than those of the wet-case, and the oceanic CBL was in a quasi-steady state; there was no diurnal variation such as that found in the wet-case in the present study. Therefore, CBL processes over humid terrestrial areas are similar to those over tropical oceanic areas with respect to the large contribution of moisture to buoyancy, but also have diurnal variation caused by the larger surface flux. These characteristics should be applicable to dry (no condensation) CBL over large paddy fields in the eastern part of China, which receive enormous latent heat flux and small sensible heat flux in early summer.

6.3 *The characteristics of forced and active cumulus boundary layers*

In the control experiment for the cumulus boundary layer, the boundary layer showed the transition from the dry CBL to the forced cumulus boundary layer and to the active cumulus boundary layer.

Features, including onset, of the forced cumulus boundary layer resembled those in previous studies (e.g., Wilde et al., 1985; Zhu and Albrecht, 2003). When the forced cumuli were generated, the mean LCL was still higher than the inversion height (Figs. 20 and 21). The updrafts were generated near the surface and involved large amounts of water vapor. These updrafts with higher relative humidity and lower LCLs than the surrounding atmosphere

produced the forced cumulus clouds (Fig. 22). As described by Zhu and Albrecht (2003), the cloud water flux was much smaller than the water vapor flux (Fig. 23b). However, the upward cloud water flux was equivalent to the downward flux of liquid water potential temperature. The cloud water carried by the forced cumulus clouds was small but important in terms of increasing the inversion height. The water vapor flux divergence in the subcloud layer was smaller than that reported by Zhu and Albrecht (2003) despite the similar moisture difference across the inversion. The difference between our results and theirs can be explained by the relatively larger amount of water vapor supplied from the surface paddy fields in this study. The amount of water vapor in the subcloud layer is determined in the balance between the water vapor supply from the surface and the rate of increase in the inversion height. Because the increasing rate of the inversion height is basically attributable to surface buoyancy flux (Tennekes, 1973), the amount of water vapor at a certain height depends on the surface energy partition.

Both forced and active cumulus existed after active cumulus onset. Whereas the forced cumulus showed a single peak of cloud fraction, the active cumulus tended to have an additional second peak (or inflection point) at the bottom of the inversion layer where most cumulus became negatively buoyant (Fig. 23). The cloud water flux largely contributed not only to total water flux but also to liquid water potential temperature flux. These vertical flux profiles reflect the mean behavior of active cumulus (cf. Stevens, 2007). Cumulus maintain positive buoyancy in the cloud layer due to condensation heating. Updrafts carry the warm, moist, and cloudy air upward (increasing cloud water, heat, and buoyancy flux in the cloud layer). After entering the inversion layer, cumulus clouds lose buoyancy and liquid water evaporates actively (decreasing cloud water, heat, and buoyancy flux in the inversion layer). Although the exchange of cloudy air for the surrounding atmosphere occurs continu-

ously, the net transport of the liquid water from the cloud layer to the inversion layer leads to liquid water potential temperature flux (entalpy flux) convergence in the cloud layer and divergence in the inversion layer. These characteristics are similar to those of the trade wind cumulus boundary layer (e.g., Siebesma and Cuijpers, 1995; Stevens et al., 2001; Siebesma et al., 2003) and the shallow cumulus described by Brown et al. (2002). The characteristics are common for the active cumulus boundary layer and are quite different from those of the forced cumulus boundary layer in terms of cloud water contribution.

6.4 *The transition from forced to active cumulus boundary layer*

One of the main focuses of this study is the onset process of active cumulus over land. The results show that active cumulus onset almost coincided with the large decrease in the LFC. The LFC drop was caused by the equivalent potential temperature of air near the surface $\overline{\theta_e(z_s)}$ becoming equal to the local minimum value of the saturated equivalent potential temperature at the bottom of the inversion layer $\overline{\theta_e^*(z_{ib})}$ (Fig. 24). The $\overline{\theta_e(z_s)}$ increased because of the increase in potential temperature in the subcloud layer. When water vapor convergence occurs in the subcloud layer, the increase in $\overline{\theta_e(z_s)}$ should be significant. On the other hand, $\overline{\theta_e^*(z_{ib})}$ decreased with the increase in the inversion height.

The cause of the appearance of the local minimum of saturated equivalent potential temperature is illustrated in Fig. 36, which shows saturated equivalent potential temperature and its components at 12 LST. By definition (Eq. 11), the saturated equivalent potential temperature θ_e^* equals the dry potential temperature θ_d multiplied by $\exp(q_{vs}L_v/c_{pd}T)$. The shape of the dry potential temperature profile (broken line) is similar to that of the potential temperature profile, consisting of an inversion layer and a well-mixed subcloud layer. Temperature (dotted line) is constrained by the shape of the potential temperature because

$T = \theta(p/p_0)^{R_d/c_{pd}}$. Therefore, the temperature lapse rate is large in the subcloud layer and relatively small in the inversion layer. The shape of the profile of $\exp(q_{vs}L_v/c_{pd}T)$ (dot-dashed line) is similar to that of the temperature profile, because $q_{vs}L_v/c_{pd}T$ mainly depends on $q_{vs}(T)$ in the numerator and not T in the denominator (as an example, the reduction ratio with 303.15 K $\rightarrow$ 293.15 K [3%] is much smaller than that with q_{vs}(30 ^{o}C, 1000 hPa) = 27.69 g kg^{-1} $\rightarrow$ q_{vs}(20 ^{o}C, 850 hPa) = 17.66 g kg^{-1} [36%]). L_v in the numerator also decreases with T. Consequently, saturated equivalent potential temperature (solid line) decreases with height in the subcloud layer due to the decrease in $\exp(q_{vs}L_v/c_{pd}T)$ and increase in the inversion layer due to the increase in the dry potential temperature. The local minimum of saturated equivalent potential temperature is yielded as a natural result of the well-mixed and inversion layers. The value decreases with increased inversion height because temperature decreases with height.

Does the active cumulus onset always coincide with the LFC drop? The LFC drop occurred in all the simulations in the present study. However, when we assume extremely weak inversion and $\partial\theta_e^*/\partial z < 0$ just above the inversion, the local minimum of $\overline{\theta_e^*}$ does not appear. The LFC is determined only by the increase in $\overline{\theta_e(z_s)}$, and thus the active cumulus onset should occur without the LFC drop. Even for this exceptional case, saturated equivalent potential temperature at the inversion height remains important for active cumulus onset, because the inversion is close to the maximum height reachable by forced cumulus.

6.5 *The cumulus boundary layer in a variety of environment including humid terrestrial area*

The sensitivity experiments showed the interaction between the cumulus boundary layer and the environment. The development of the cumulus boundary layer was largely affected by external factors such as the initial amount of water vapor, static stability, and surface energy partition. On the other hand, the development of the cumulus boundary layer involved variation in the vertical water vapor distribution, because the water vapor supplied from the surface is distributed into ranges from the surface to the inversion height. The inversion height is determined by its rate of increase. As mentioned above, the active cumulus boundary layer created a larger rate of increase in inversion height than did the dry convective and forced cumulus boundary layers. Therefore, the occurrence of active cumulus onset and its timing during the day are important for determining the final (evening) inversion height.

A larger amount of initial water vapor resulted in a higher inversion height (Figs. 27 and 31). The initial water vapor directly contributed to the initial value of $\overline{\theta_e(z_s)}$, which is a function of water vapor. The decrease in $\overline{\theta_e^*(z_{ib})}$ also became larger due to the earlier onset of the forced cumulus and slightly deeper inversion height. Thus, the timing of active cumulus onset [i.e., the time satisfying $\overline{\theta_e(z_s)} > \overline{\theta_e^*(z_{ib})}$] became earlier due to the contributions of both $\overline{\theta_e(z_s)}$ and $\overline{\theta_e^*(z_{ib})}$. In addition, the active cumulus boundary layer developed at a slightly larger rate. Consequently, higher inversion height was obtained.

Smaller static stability led to large rates of increase in the inversion height in all stages. Although the thick dry convective and forced cumulus boundary layers were disadvantageous for the increase in $\overline{\theta_e(z_s)}$, they led to the decrease in $\overline{\theta_e^*(z_{ib})}$ and earlier active cumulus onset. The earlier active cumulus onset and larger development rate produced the large increase in

the inversion height.

The greater surface evaporative efficiency yielded smaller Bowen ratios and decreased the rate of inversion height increase in the dry convective and forced cumulus boundary layers because of the smaller surface buoyancy flux. Although the decrease in $\overline{\theta_e^*(z_{ib})}$ became smaller, the increase in $\overline{\theta_e(z_s)}$ became larger because of the larger amount of water vapor supply. Because the effect of $\overline{\theta_e(z_s)}$ overcame that of $\overline{\theta_e^*(z_{ib})}$, active cumulus onset occurred earlier. The development rate of the active cumulus boundary layer was almost the same. Decrease in the Bowen ratio yielded both high and low inversion heights, depending on the initial water vapor and static stability.

The water vapor distribution changed mainly below the inversion height (Fig. 35). The shapes of water vapor profiles were different between cases with and without active cumulus. The active cumulus yielded a cloud layer and thickened the cloud layer over time. Active cumulus also transported total water from the subcloud layer to the inversion layer and simultaneously inhibited the increase in water vapor in the subcloud layer. Therefore, in the cases with active cumulus, increases in water vapor amounts were large at higher levels but small at lower levels. In contrast, in the cases without active cumulus, a large amount of water vapor was accumulated in the subcloud layer. This effect of active cumulus on water vapor profiles should be important in convective instability.

Active cumulus onset coincided with a decrease in the rate of increase in the total cloud fraction (Figs. 20 and 33). Although the total cloud fraction kept increasing until active cumulus onset, it showed a nearly constant value or started to decrease after the onset of active cumulus. According to Wilde et al. (1985), the total cloud fraction of forced cumulus increases the lower LCL and leads to higher inversion height that causes higher relative humidity in the inversion layer. In the present cases, the active cumulus transported

total water higher and appeared to inhibit the increase in relative humidity at the top of the subcloud layer. The effects of active cumulus onset on the time tendency of total cloud fraction should be investigated further, with consideration of cloud tilting caused by horizontal wind shear as described by Hinkelman et al. (2005).

The himid terrestrial area is characterized by the small Bowen raio and large amount of water vapor in the lower troposphere. In such condition, the onset of active cumulus is more likely to occur. Therefore, the onset time and vertical fluxes of the active cumulus boundary layer should be important for the change of the vertical water vapor distribution in the humid terrestrial area.

7 Summary and Conclusions

Although many previous studies have examined the CBL over relatively dry terrestrial areas, few have examined CBL processes in detail over humid terrestrial areas. The aim of this study was to clarify the development of the dry convective boundary layer and cumulus boundary layer over a humid terrestrial area: the Huaihe River Basin of China. Data for early summer 2004 were obtained from flux tower and WPR observations during the IOP-2004 of the LAPS project, and high-resolution numerical simulations using the CReSS model were performed.

The IOP-2004 was divided into two periods according to the condition of the surface vegetation. In the first period, mature wheat fields or bare fields provided almost the same amounts of sensible and latent heat fluxes. In the second period, paddy fields provided small sensible heat flux and enormous latent heat flux. Two clear days (31 May and 22 June 2004) were selected as typical cases for each period and identified as the dry-case and the wet-case, respectively. For the dry-case, the sensible heat flux (390 W m^{-2} at maximum) was larger than the latent heat flux (300 W m^{-2} at maximum), although the difference between both was small. The CBL started to develop rapidly from 0730 LST, and the top attained a maximum height of 2250 m. For the wet-case, the sensible heat flux was slight (150 W m^{-2} at maximum), and the latent heat flux was very large (560 W m^{-2} at maximum). The development of the CBL started slowly at 1000 LST, and the maximum height was 1400 m. The updrafts in the CBL were strong for the dry-case (3 m s^{-1}) and weak for the wet-case (1.5 m s^{-1}).

The simulations were conducted to investigate the three-dimensional structure of the CBL, including the temperature and humidity, and to evaluate the vertical fluxes caused by

the circulation in the CBL. The surface heat fluxes and the development of the CBL for both the dry-case and the wet-case were adequately reproduced. The vertical velocity showed a correlation with potential temperature and the mixing ratio of water vapor, indicating vertical transport of heat and moisture. The vertical heat and moisture fluxes in the CBL were also estimated. For the dry-case, heat contributed nearly all of the buoyancy flux, as in previous studies of relatively dry terrestrial areas. For the wet-case, on the other hand, the contribution of moisture was equal to that of heat. In particular in late afternoon, the moisture contribution yielded most of the positive value of the buoyancy flux. The results suggest that the large contribution of moisture to the buoyancy is a characteristic of the CBL in humid terrestrial areas.

Further, the development of the cumulus boundary layer over humid terrestrial area was investigated using the high-resolution numerical simulations with the focus on the onset of the positively boyant active cumulus which has been given less attention than that of forced cumulus and deep precipitating cumulus.

The initial profile was idealized as virtual potential temperature constantly increasing with height and water vapor exponentially decreasing with height. Parameters for the idealized initial profile and land surface for the control experiment were set using observations made on 20 June 2004 in the Huaihe River Basin of China. In addition, systematic sensitivity experiments were performed by varying the initial water vapor, static stability, and surface energy partition parameters.

For the control experiment, the boundary layer evolved from the dry CBL to the forced cumulus boundary layer and to active cumulus boundary layer. The characteristics in the each stage were consistent with those of previous studies. The dry CBL began to develop at 08 LST, and cumulus clouds appeared at 0920 LST. Until around 12 LST, the cloud

fraction showed a single peak just above the cloud base height. The profiles of virtual potential temperature and water vapor were constant (well mixed), and relative humidity increased with height below the inversion. According to the vertical section and fraction of positive-buoyancy cloud elements, the virtual potential temperature in the cumulus cloud was lower than that of the surrounding atmosphere at 11 LST. No cumulus clouds in the fields had positive buoyancy, and therefore these clouds were identified as forced cumulus. The vertical fluxes were almost similar to the features of the dry CBL except for the small enhancement of the negative liquid water potential temperature flux by the contribution of cloud water flux in the inversion layer. The LFC derived from mean values near the land surface was higher than 2700 m at 1210 LST; however, it suddenly decreased to 1100 m at 1220 LST. The structure of the cumulus boundary layer changed after the LFC drop. The cloud fraction tended to show a second peak just below the inversion height. In the cloud layer, the profile of virtual potential temperature (water vapor) had a positive (negative) gradient, and relative humidity remained nearly constant with height. Active cumulus with a higher virtual potential temperature than the surrounding atmosphere also existed at 13 LST. According to the vertical fluxes, the active cumulus essentially contributed to the total water and enthalpy fluxes; the active cumulus transported total water from the subcloud layer to the inversion layer, and heated the cloud layer and cooled the inversion layer.

The LFC drop was almost coincident with active cumulus onset. With the development of the dry convective and forced cumulus boundary layers, the equivalent potential temperature gradually increased in the boundary layer because of surface fluxes. On the other hand, local minimum value of saturated equivalent potential temperature was produced at the bottom height of the inversion layer as a result of the potential temperature profile consisting of well-mixed and inversion layers. This local minimum value rapidly decreased with the increase in

the inversion height. The LFC drop occurred when the equivalent potential temperature of the air near the surface $\overline{\theta_e(z_s)}$ became larger than the local minimum of saturated equivalent potential temperature at the bottom of the inversion layer $\overline{\theta_e^*(z_{ib})}$.

The sensitivity experiments demonstrated the interaction between the cumulus boundary layer and environmental conditions. The active cumulus onset time became earlier with 1) greater initial water vapor, 2) smaller static stability, and 3) greater surface evaporative efficiency. The cause of the time advance is attributed to change in the time tendencies of $\overline{\theta_e^*(z_{ib})}$ and $\overline{\theta_e(z_s)}$. 1) The greater initial water vapor contributed directly to the increase in initial $\overline{\theta_e(z_s)}$. In addition, the earlier forced cumulus onset led to slightly higher inversion height and consequently smaller $\overline{\theta_e^*(z_{ib})}$. Thus, both larger $\overline{\theta_e(z_s)}$ and smaller $\overline{\theta_e^*(z_{ib})}$ are favorable for the onset of active cumulus. Because the inversion height showed large rates of increase after active cumulus onset, earlier active cumulus onset led to a higher inversion height. 2) Smaller static stability made the boundary layer deeper in all stages. The deep boundary layer was disadvantageous for the increase in $\overline{\theta_e(z_s)}$ because limited water vapor was distributed in the deep boundary layer. However, the fast decrease in $\overline{\theta_e^*(z_{ib})}$ yielded earlier active cumulus onset. The inversion height then increased owing to the earlier active cumulus onset and larger development rate. 3) The greater evaporative efficiency yielded larger latent and smaller sensible heat fluxes (smaller Bowen ratio). Both fluxes induced the increase in $\overline{\theta_e(z_s)}$, because large amounts of water vapor were supplied to the shallow dry convective and forced cumulus boundary layers. Consequently, the active cumulus onset occurred earlier despite the smaller decrease in $\overline{\theta_e^*(z_{ib})}$. Although the inversion height was lower before the active cumulus onset, it reached a similar level in evening because of the earlier active cumulus onset.

The higher inversion height corresponded to the deeper moist layer. However, it resulted

in a smaller increase in the amount of water vapor because a limited amount of water vapor was distributed in the deeper layer. Thus, even for the same water vapor supply, the water vapor profile and convective instability changed with the development of the cumulus boundary layer. The total cloud fraction began to decrease or stopped increasing at the time of active cumulus onset. The change in the time tendency of the total cloud fraction is attributed to the effect of water vapor transport by active cumulus; active cumulus transported water vapor higher and suppressed the increase in relative humidity at the top of the subcloud layer. The active cumulus onset is an important threshold for the development of the cumulus boundary layer and the change of the atmospheric condition over land, particularly in humid terrestrial area that the large amount of water vapor and small Bowen ratio are predominant.

Acknowledgments

I would like to express my special thanks to my supervisor Dr. T. Shinoda (Hydrospheric Atmospheric Research Center (HyARC), Nagoya University) for his instruction, suggestion and encouragement. I would like to express my gratitude to Prof. H. Uyeda, Prof. K. Nakamura, Dr. K. Tsuboki (HyARC, Nagoya University) for their helpful suggestion and support. I am grateful to Dr. H. Tanaka and Dr. Hiyama (HyARC, Nagoya University) for their encouragement and valuable comments. I express my thanks to Mr. A. Sakakibara (Chuden CTI, Ltd.) for his help in using the CReSS model. I would like to acknowledge Dr. A. Higuchi (Chiba University), Dr. H. Fujinami, Mr. K. Yamamoto (HyARC, Nagoya University) and Mr. S. Ikeda (Okayama University) for conducting the observations. I want to thank the members of the LAPS project, Laboratory of Meteorology and Laboratory of Eco-Hydrometeorology of HyARC, Nagoya University, for their kind encouragement and helpful support. The author was grateful to Sumitomo Electric Industries, Ltd., and Climatec, Inc. for the installation and maintenance of the observation equipment and to Shouxian Meteorological Observatory, Anhui Meteorological Bureau, and the China Meteorological Administration (CMA) for their support in performing the observations. The simulations were performed at the Information Technology Center of the University of Tokyo. The sounding data were obtained from the University of Wyoming. This study was supported by the Core Research for Evolutional Science and Technology (CREST) program of the Japan Science and Technology Agency (JST). The author was partly supported by the 21st Century COE Program "Dynamics of the Sun-Earth-Life Interactive System" (SELIS) of Nagoya University. Generic Mapping Tools (GMT) software was used to draw the figures.

References

Angevine, W. M., A. B. White and S. K. Avery, 1994: Boundary-layer depth and entrainment zone characterization with a boundary-layer profiler. *Bound.-Layer. Meteor.*, **68**, 375–385.

Beyrich, F. and U. Görsdorf, 1995: Composing the diurnal cycle of mixing height from simultaneous sodar and wind profiler measurements. *Bound.-Layer. Meteor.*, **76**, 387–394.

Brown, A. R., R. T. Cederwall, A. Chlond, P. G. Duynkerke, J.-C. Golaz, M. Khairoutdinov, D. C. Lewellen, A. P. Lock, M. K. MacVean, C.-H. Moeng, R. A. J. Neggers, A. P. Siebesma and B. Stevens, 2002: Large-eddy simulation of the diurnal cycle of shallow cumulus convection over land. *Q. J. R. Meteorol. Soc.*, **128**, 1075–1093.

Cohn, S. A. and W. M. Angevine, 2000: Boundary layer height and entrainment zone thickness measured by lidars and wind-profiling radars. *J. Appl. Meteor.*, **39**, 1233–1247.

Crum, T. D., R. B. Stull and E. W. Eloranta, 1987: Coincident lidar and aircraft observations of entrainment into thermals and mixed layers. *J. Clim. Appl. Meteor.*, **26**, 774–788.

Ecklund, W. L., D. A. Carter and B. B. Balsley, 1988: A UHF wind profiler for the boundary layer: Brief description and initial results. *J. Atmos. Ocean. Technol.*, **5**, 432–441.

Emanuel, K. A., 1994: *Atmospheric Convection*. Oxford Univ. Press., 580pp.

Garratt, J. R., 1992: *The Atmospheric Boundary Layer*. Cambridge Univ. Press., 316pp.

Grimsdell, A. W. and W. M. Angevine, 1998: Convective boundary layer height measurement with wind profilers and comparison to cloud base. *J. Atmos. Ocean. Technol.*, **15**, 1331–1338.

Hashiguchi, H., M. D. Yamanaka, T. Tsuda, M. Yamamoto, T. Nakamura, T. Adachi and S. Fukao, 1995: Diurnal variations of the planetary boundary layer observed with an L-band clear-air Doppler radar. *Bound.-Layer. Meteor.*, **74**, 419–424.

Hinkelman, L. M., B. Stevens and K. F. Evans, 2005: A large-eddy simulation study of anisotropy in fair-weather cumulus cloud fields. *J. Atmos. Sci.*, **62**, 2155–2171.

Kaimal, J. C. and J. J. Finnigan, 1994: *Atmospheric Boundary Layer Flows -Their Structure and Measurement-*. Oxford Univ. Press., 289pp.

Kaimal, J. C., J. C. Wyngaard, D. A. Haugen, O. R. Coté and Y. Izumi, 1976: Turbulence structure in the convective boundary layer. *J. Atmos. Sci.*, **33**, 2152–2169.

Khairoutdinov, M. and D. Randall, 2006: High-resolution simulation of shallow-to-deep convection transition over land. *J. Atmos. Sci.*, **63**, 3421–3436.

Kim, W., T. Arai, S. Kanae, T. Oki and K. Musiake, 2001: Application of the Simple Biosphere Model (SiB2) to a paddy field for a period of growing season in GAME-Tropics. *J. Meteor. Soc. Japan*, **79**, 387–400.

Kollias, P., B. A. Albrecht, R. Lhermitte and A. Savtchenko, 2001: Radar observations of updrafts, downdrafts, and turbulence in fair-weather cumuli. *J. Atmos. Sci.*, **58**, 1750–1766.

Liu, A. Q., G. W. K. Moore, K. Tsuboki and I. A. Renfrew, 2006: The effect of the sea-ice zone on the development of boundary-layer roll clouds during cold air outbreaks. *Bound.-Layer. Meteor.*, **118**, 557–581.

Louis, J. F., M. Tiedtke and J. F. Geleyn, 1981: A short history of the operational PBL parameterization at ECMWF. *ECMWF Workshop on Planetary Boundary Layer Parameterization*, 59–79, Reading, UK, ECMWF.

Loveland, T. R., B. C. Reed, J. F. Brown, D. O. Ohlen, J. Zhu, L. Yang and J. W. Merchant, 2000: Development of a global land cover characteristics database and IGBP DISCover from 1-km AVHRR data. *Int. J. Rem. Sens.*, **21**, 1301–1330.

Maesaka, T., G. W. K. Moore, Q. Liu and K. Tsuboki, 2006: A simulation of a lake effect snowstorm with a cloud resolving numerical model. *Geophys. Res. Lett.*, **33**, L20813.

Nicholls, S. and M. A. LeMone, 1980: The fair weather boundary layer in GATE: The relationship of subcloud fluxes and structure to the distribution and enhancement of cumulus clouds. *J. Atmos. Sci.*, **37**, 2051–2067.

Nishikawa, M., T. Hiyama, K. Tsuboki and Y. Fukushima, 2009: Numerical simulations of local circulation and cumulus generation over the Loess Plateau, China. *J. Appl. Meteor. Climatol.*, **48**, 849–862.

Oue, H., 2005: Influence of meteorological and vegetational factors on the partitioning of the energy of a rice paddy field. *Hydorol. Process.*, **19**, 1567–1583.

Shinoda, T. and H. Uyeda, 2002: Effective factors in the development of deep convective clouds over the wet region of eastern China during the summer monsoon season. *J. Meteor. Soc. Japan*, **80**, 1395–1414.

Shinoda, T., H. Uyeda and K. Yoshimura, 2005: Structure of moist layer and sources of water over the southern region far from the Meiyu/Baiu fornt. *J. Meteor. Soc. Japan*, **83**, 137–152.

Shusse, Y. and K. Tsuboki, 2006: Dimension characteristics and precipitation efficiency of cumulonimbus clouds in the region far south from the Mei-Yu front over the eastern Asian continent. *Mon. Wea. Rev.*, **134**, 1942–1953.

Shusse, Y., K. Tsuboki, B. Geng, H. Minda and T. Takeda, 2005: Structure and evolution of deeply developed convective cells in a long-lived cumulonimbus cloud under a weak vertical wind-shear condition. *J. Meteor. Soc. Japan*, **83**, 351–371.

Siebesma, A. P. and J. W. M. Cuijpers, 1995: Evaluation of parametric assumptions for shallow cumulus convection. *J. Atmos. Sci.*, **52**, 650–666.

Siebesma, A. P., C. S. Bretherton, A. Brown, A. Chlond, J. Cuxart, P. Duynkerke, H. Jiang, M. Khairoutdinov, D. Lewellen, C.-H. Moeng, E. Sanchez, B. Stevens and D. E. Stevens, 2003: A large-eddy simulation intercomparison study of shallow cumulus convection. *J. Atmos. Sci.*, **60**, 1201–1219.

Stevens, B., 2007: On the growth of layers of nonprecipitating cumulus conection. *J. Atmos. Sci.*, **64**, 2916–2931.

Stevens, B., A. S. Ackerman, B. A. Albrecht, A. R. Brown, A. Chlond, J. Cuxart, P. G. Duynkerke, D. C. Lewellen, M. K. Macvean, R. A. J. Neggers, E. Sánchez, A. P. Siebesma and D. E. Stevens, 2001: Simulations of trade wind cumuli under a strong inversion. *J. Atmos. Sci.*, **58**, 1870–1891.

Stull, R. B., 1985: A fair-weather cumulus cloud classification scheme for mixed-layer studies. *J. Climate App. Meteor.*, **24**, 49–56.

Stull, R. B., 1988: *An Introduction to Boundary Layer Meteorology*. Kluwer Academic Publishers, 666pp.

Tanaka, K., 2004: *Development of the new land surface scheme SiBUC commonly applicable to basin water management and numerical weather prediction model*. Doctoral dissertation, Kyoto Univ.

Tanaka, H., T. Hiyama, K. Yamamoto, H. Fujinami, T. Shinoda, A. Higuchi, S. Endo, S. Ikeda, W. Li and K. Nakamura, 2007: Surface flux and atmospheric boundary layer observations from the LAPS project over the middle stream of the Huaihe River Basin in China. *Hydro. Process.*, **21**, 1997–2008, DOI: 10.1002/hyp.6706.

Tennekes, H., 1973: A model for the dynamics of the inversion above a convective boundary layer. *J. Atmos. Sci.*, **30**, 558–567.

Tsuboki, K. and A. Sakakibara, 2002: Large-scale parallel computing of Cloud Resolving Storm Simulator. H. P. Zima and et al., Eds., *High Performance Computing*, Springer, 243–259.

White, A. B., C. W. Fairall and D. W. Thomson, 1991: Radar observation of humidity variability in and above the marine atmospheric boundary layer. *J. Atmos. Oceanic Technol.*, **8**, 639–658.

Wilde, N. P., R. B. Stull and E. W. Eloranta, 1985: The LCL zone and cumulus onset. *J. Clim. Appl. Meteor.*, **24**, 640–657.

Yi, C., K. J. Davis and B. W. Berger, 2001: Long-term observations of the continental planetary boundary layer. *J. Atmos. Sci.*, **58**, 1288–1299.

Young, G. S., 1988a: Turbulence structure of the convective boundary layer. Part I: Variability of normalized turbulence statistics. *J. Atmos. Sci.*, **45**, 719–726.

Young, G. S., 1988b: Turbulence structure of the convective boundary layer. Part Ⅱ: PHOENIX 78 aircraft observations of thermals and their environment. *J. Atmos. Sci.*, **45**, 727–735.

Young, G. S., D. A. R. Kristovich, M. R. Hjelmfelt and R. C. Foster., 2002: Rolls, streets, waves and more: A review of quasi-two dimensional structures in the atmospheric boundary layer. *Bull. Amer. Meteor. Soc.*, **83**, 997–1001.

Zhao, B. and T. Takeda, 1998: *Huaihe River Basin Experiment (GAME/HUBEX).* Beijing Univ., 24pp.

Zhu, P. and B. Albrecht, 2003: Large eddy simulation of continental shallow cumulus convection. *J. Geophys. Res.*, **108(D15)**, 4453.

Tables

Table 1: Operating specifications of the WPR.

Frequency	1290 MHz
Antenna	Phased array
Beam width	Less than 5°
Peak power	2 kW
Pulse width	666 ns
Inter pulse period	80 μs
Gate spacing	100 m
Temporal resolution	59 s

Table 2: Configuration of the numerical simulations for the dry convective boundary layer.

Turbulence	1.5-order TKE
Surface	Bulk method (Louis et al., 1981) Calculation of soil temperature: 0.1 m × 30 levels
Cloud microphysics	Bulk method of warm rain
Radiation	Only surface energy balance
No. of grid points (Domain)	Horizontal: 200 × 200 (20 km × 20 km) Vertical: 120 ($\simeq$ 5888 m)
Resolution	Horizontal: 100 m Vertical: 30 m (Streched by *tanh* above 3000 m)
Lateral boundary	Periodic boundary conditions
Top boundary	Rigid boundary conditions Sponge layer above 3000 m
Bottom boundary	Configurated as the land surface (cf. Table.3)
Forcing	Shortwave radiation with diurnal variation
Initial conditions	Idealized profile with θ perturbation (see text)
Integrated time	12 h (08 - 20 LST)

Table 3: Land surface parameters for the numerical simulations for the dry convective boundary layer.

	Bare fields (dry-case: 31 May)	Paddy fields (wet-case: 22 June)
Albedo	0.14	0.11
Moisture availability	0.06	0.40
Roughness length for momentum	0.1 m	0.1 m
Roughness length for heat	0.1 m	0.1 m
Soil temperature at the deepest layer	293 K	296 K
Heat capacity of soil	2.3×10^6 J m^{-3} K^{-1}	3.0×10^6 J m^{-3} K^{-1}
Thermal diffusivity	7.0×10^{-7} m^2 s^{-1}	7.0×10^{-7} m^2 s^{-1}

Table 4: Configuration of the numerical experiments of the cumulus boundary layer.

Turbulence	1.5-order TKE
Surface	Bulk method (Louis et al., 1981) Calculation of soil temperature: 0.1 m × 30 levels
Cloud microphysics	Bulk method of warm rain
Radiation	Only surface energy balance Diagnostics of cloud effect
No. of grid points (Domain)	Horizontal: 200 × 200 (20 km × 20 km) Vertical: 230 ($\simeq$ 10 km)
Resolution	Horizontal: 100 m Vertical: 30 m (Streched by *tanh* above 6000 m)
Lateral boundary	Periodic boundary conditions
Top boundary	Rigid boundary conditions Sponge layer above 6000 m
Bottom boundary	Configurated as the land surface (cf. Table.5)
Forcing	Shortwave radiation with diurnal variation
Initial conditions	Idealized profile with θ perturbation (see text)
Integrated time	14 h (06 - 20 LST)

Table 5: Land surface parameters for the control experiment of the cumulus boundary layer.

Albedo	0.11
Evaporative efficiency	0.25
Roughness length for momentum	0.1 m
Roughness length for heat	0.1 m
Soil temperature at the deepest layer	296 K
Heat capacity of soil	3.0×10^6 J m^{-3} K^{-1}
Thermal diffusivity	7.0×10^{-7} m^2 s^{-1}

Table 6: The relation between the parameters of initial profiles and the sensitivity experiments.

Γ_v	β	q_0 (g kg^{-1})				
(K km^{-1})		17	16	15	14	13
3.5	0.10	G35B10Q17	G35B10Q16	G35B10Q15	G35B10Q14	
3.5	0.25	G35B25Q17	G35B25Q16	G35B25Q15	G35B25Q14	
3.5	0.40	G35B40Q17	G35B40Q16	G35B40Q15	G35B40Q14	
4.5	0.10	G45B10Q17	G45B10Q16	G45B10Q15	G45B10Q14	
4.5	0.25	***G45B25Q17***	*G45B25Q16*	*G45B25Q15*	*G45B25Q14*	*G45B25Q13*
4.5	0.40	G45B40Q17	G45B40Q16	G45B40Q15	G45B40Q14	
5.5	0.10	G55B10Q17	G55B10Q16	G55B10Q15	G55B10Q14	
5.5	0.25	G55B25Q17	G55B25Q16	G55B25Q15	G55B25Q14	
5.5	0.40	G55B40Q17	G55B40Q16	G55B40Q15	G55B40Q14	

Table 7: Characteristics of the CBL for the dry-case and the wet-case.

	Dry-case (31 May)	Wet-case (22 June)
Land surface	Bare fields	Paddy fields
Surface flux	LHF $\leq$ SHF	LHF $\gg$ SHF
Starting time of the development of the CBL	0730 LST	1000 LST
Time when the CBL top reached upper limit	1400 LST	1630 LST
Highest CBL top	2250 m	1400 m
Maximum speed of updrafts	3 m s^{-1}	1.5 m s^{-1}
Horizontal scale of the circulations	3 km	1.3 km

Figures

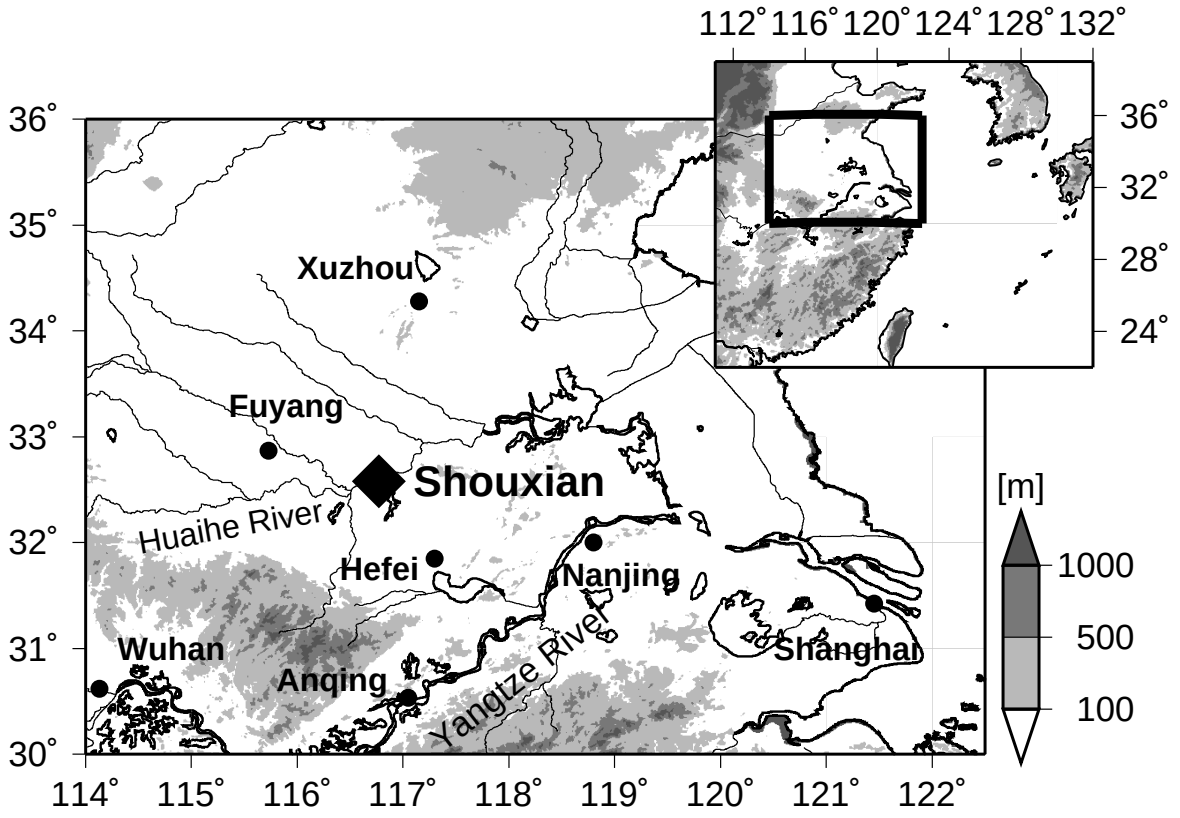

Fig. 1: Topography around the observation point, Shouxian (⧫).

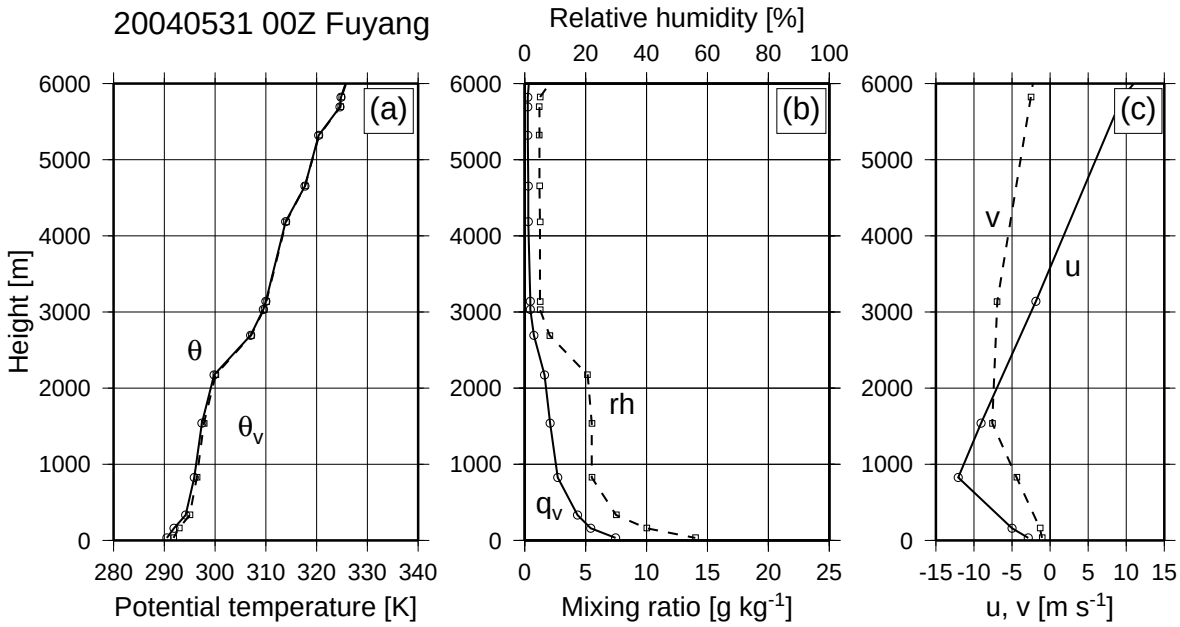

Fig. 2: Sounding profiles at Fuyang at 00 UTC (08 LST) on 31 May 2004, used as the initial condition for the numerical simulation of the dry-case. (a) Profiles of potential temperature (θ; solid line) and virtual potential temperature (θ_v; broken line). (b) Profiles of the mixing ratio of water vapor (q_v; solid line) and relative humidity (rh; broken line). (c) Profiles of zonal wind speed (u; solid line) and meridional wind speed (v; broken line).

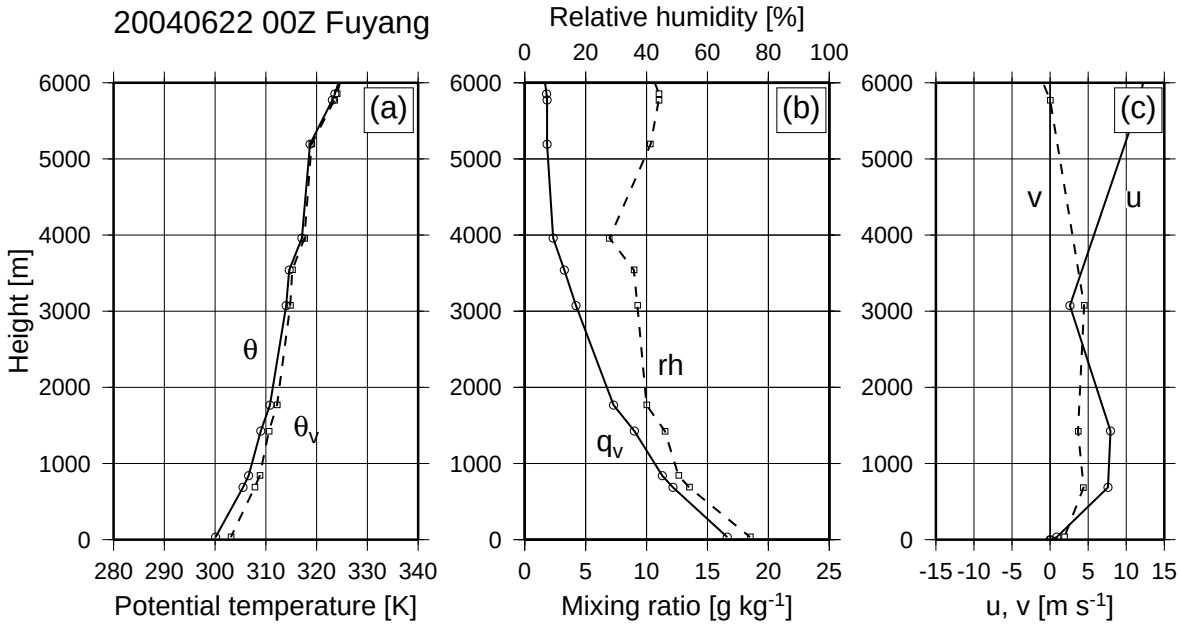

Fig. 3: The same as Fig. 2 but for 22 June 2004, used as the initial condition for the numerical simulation of the wet-case.

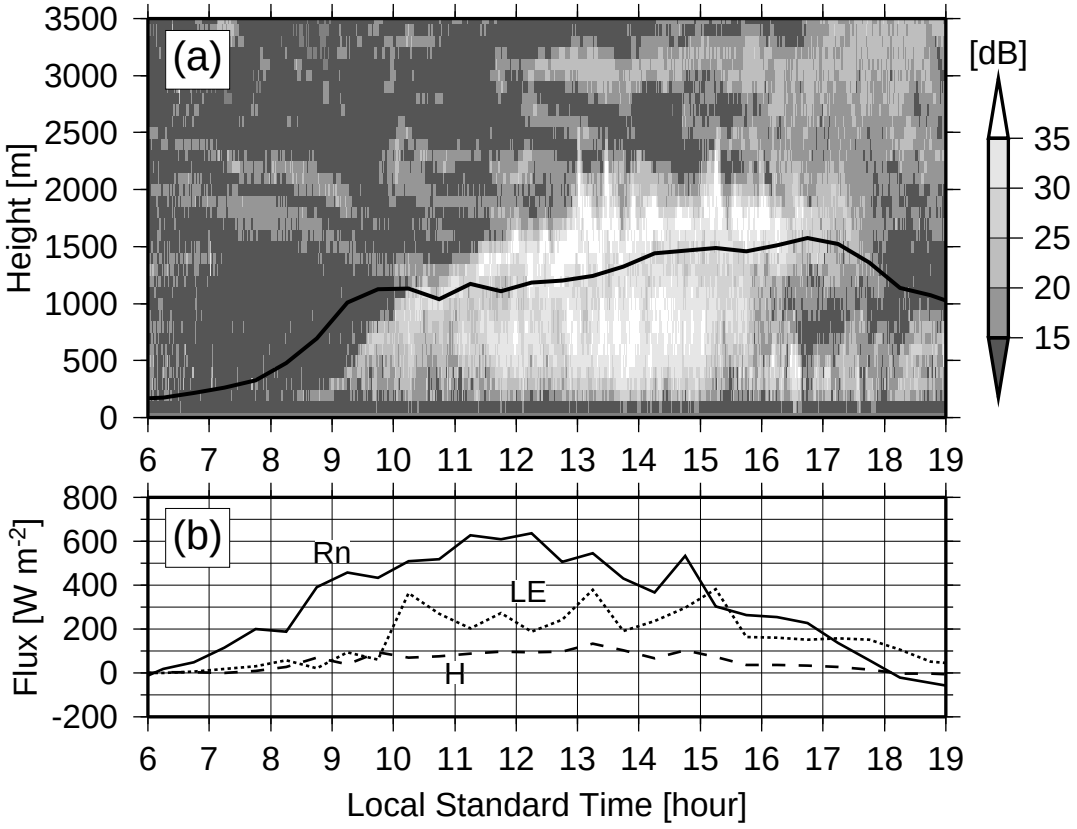

Fig. 4: (a) Time-height cross section of SNR of wind profiler radar and time series of LCL (solid line) calculated from mean values at 32 m AGL on 20 June 2004. (b) Time series of net radiation flux (solid line), sensible heat flux (broken line) and latent heat flux (dotted line) at 32 m AGL.

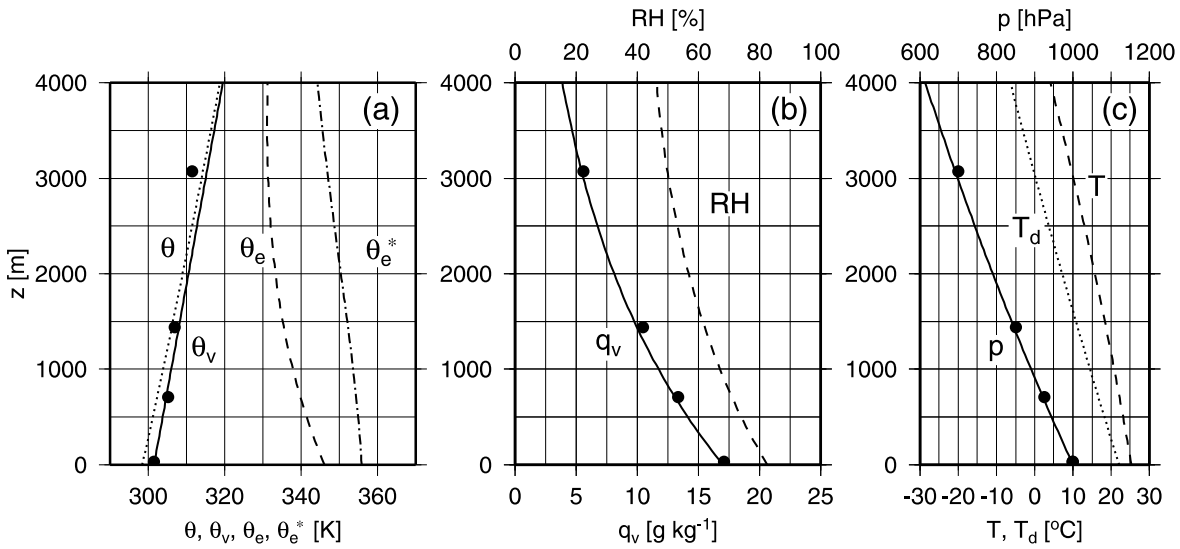

Fig. 5: Initial Profiles for the control simulation and sounding at Fuyang at 00 UTC on 20 June 2004. (a) Profiles of potential temperature θ (dotted line), virtual potential temperature θ_v (solid line), equivalent potential temperature θ_e (broken line) and saturated equivalent potential temperature θ_e^* (chain line). Circles indicate observed virtual potential temperature. (b) Profiles of water vapor mixing ratio q_v (solid line) and relative humidity RH (broken line). Circles indicate observed water vapor mixing ratio. (c) Profiles of pressure p (solid line), temperature T (broken line) and dew point temperature T_d (dotted line). Circles indicate observed pressure.

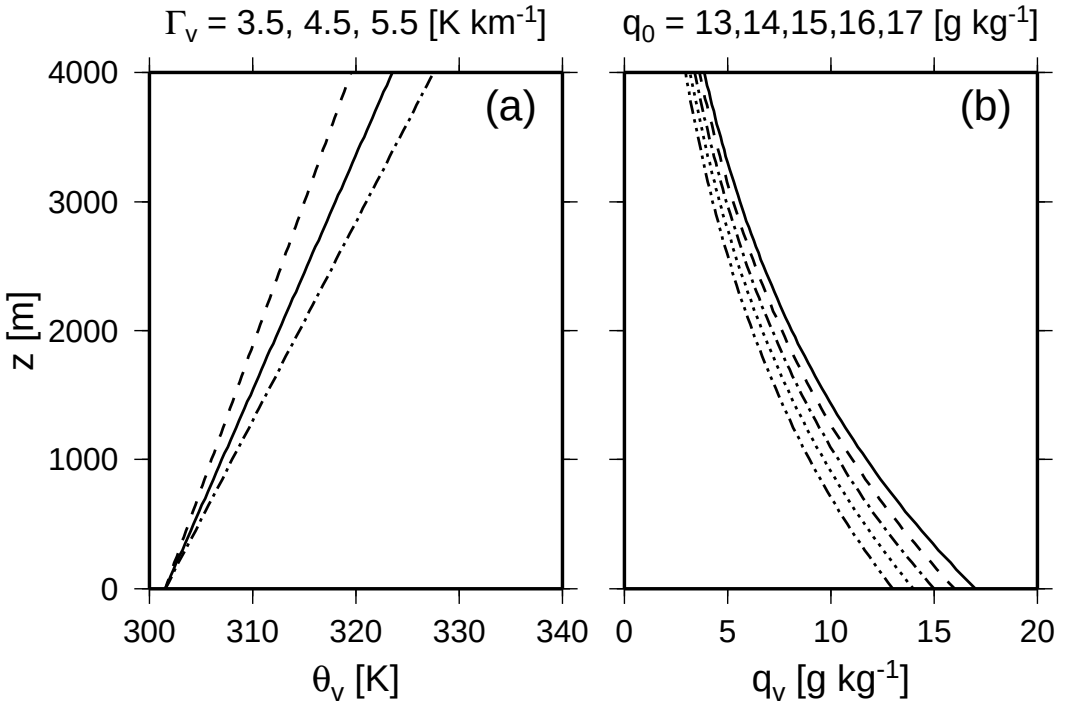

Fig. 6: Initial profiles for the sensitivity simulations. Solid line indicates the initial profile for the control simulation. (a) Profiles of virtual potential temperature corresponding to $\Gamma_v = 3.5$ (broken line), 4.5 (solid line), 5.5 (chain line) [K km^{-1}]. (b) Profiles of water vapor mixing ratio corresponding to $q_0 = 13$ (two-dot chain line), 14 (dotted line), 15 (chain line), 16 (broken line), 17 (solid line) [g kg^{-1}].

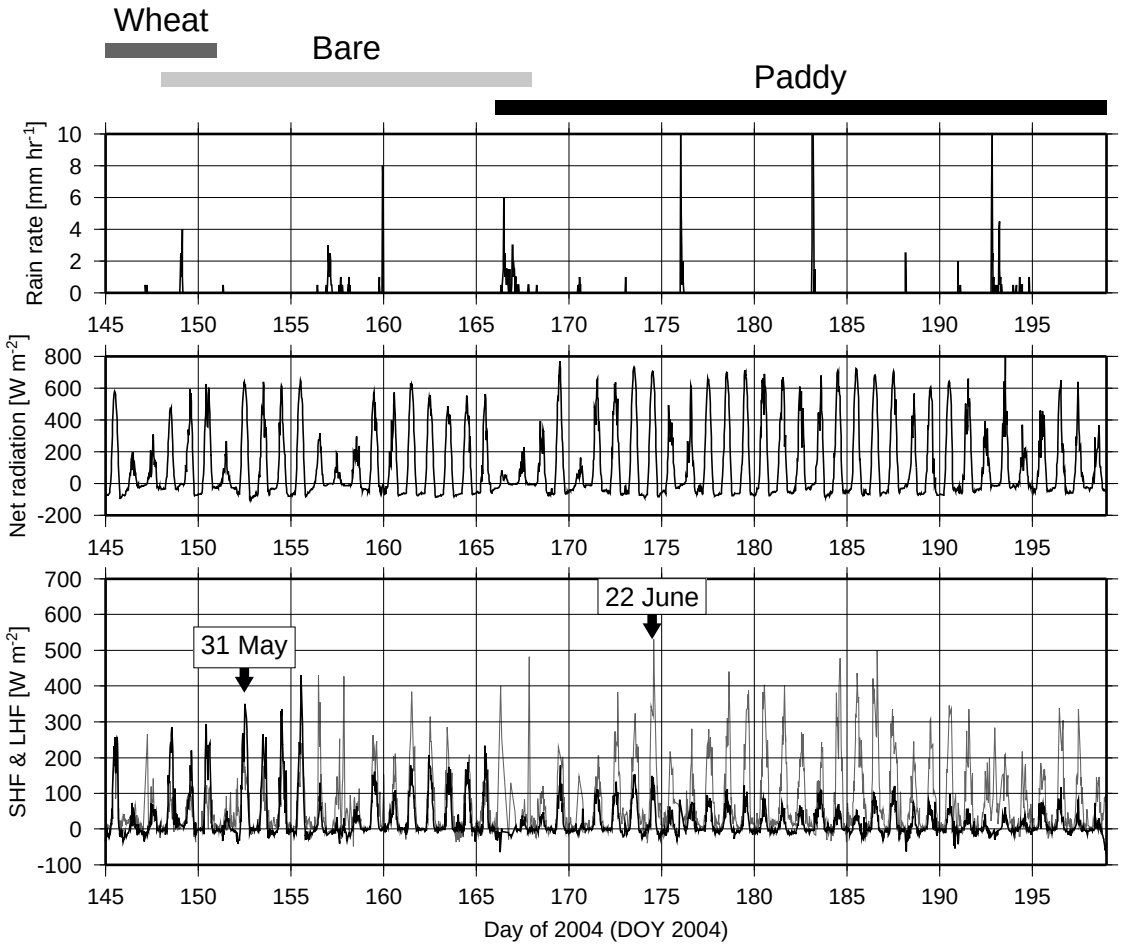

Fig. 7: Time series of the rain rate at the surface, net radiation, sensible heat flux (SHF; black line), and latent heat flux (LHF; gray line) observed at 32 m above ground level (AGL) during the IOP from 24 May [Day of Year (DOY) = 145] to 16 July (DOY = 199) 2004. "Wheat," "Bare," and "Paddy" indicate the periods when vegetation around the observation site was mature wheat field, bare field, and paddy field, respectively.

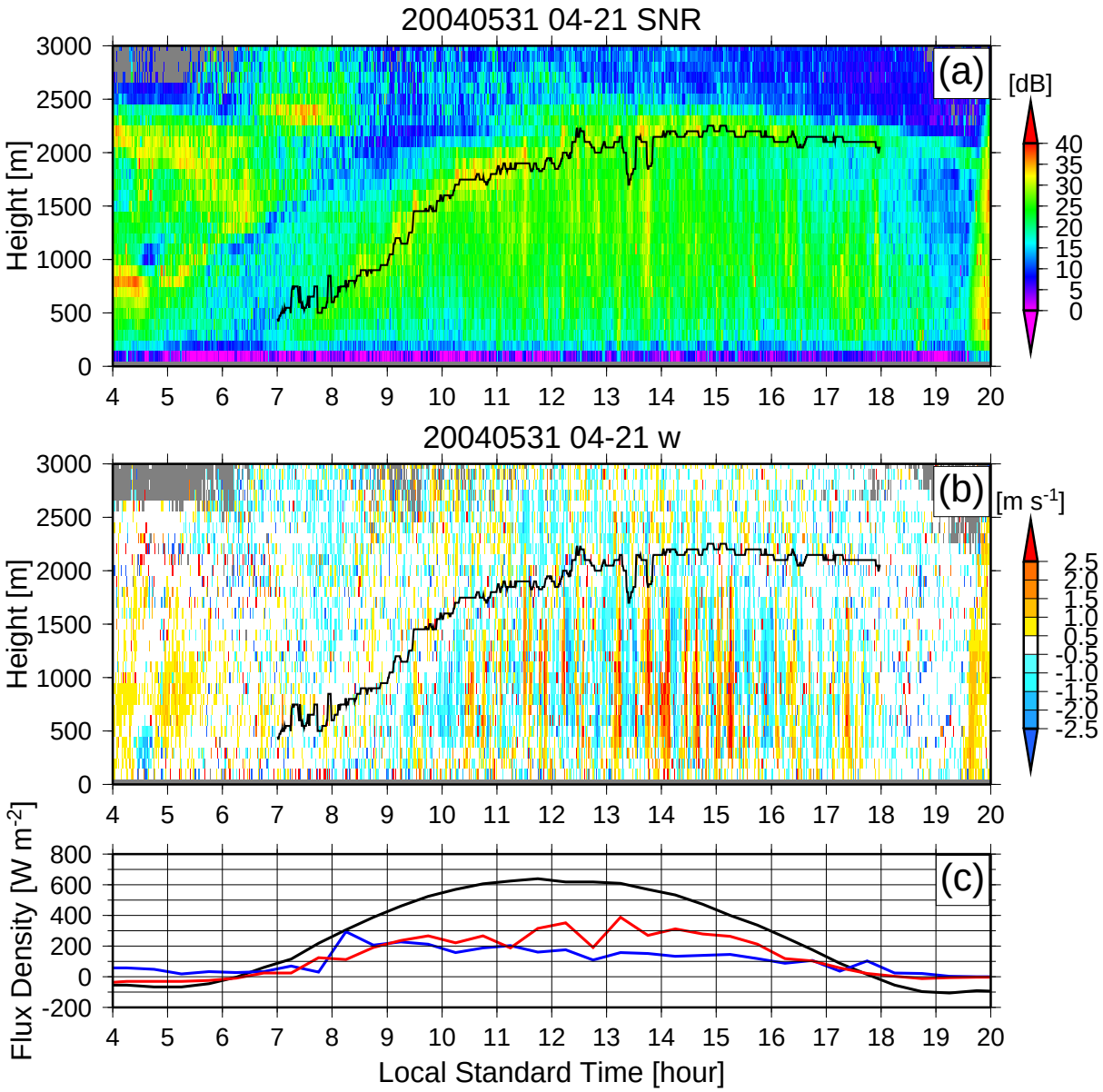

Fig. 8: (a) Time-height cross section of the SNR on 31 May 2004, referred to as the dry-case. The black line indicates the CBL top estimated from the SNR profile at the time. (b) The same as (a) but for vertical velocity. (c) Time series of net radiation (black line), sensible heat flux (red line), and latent heat flux (blue line).

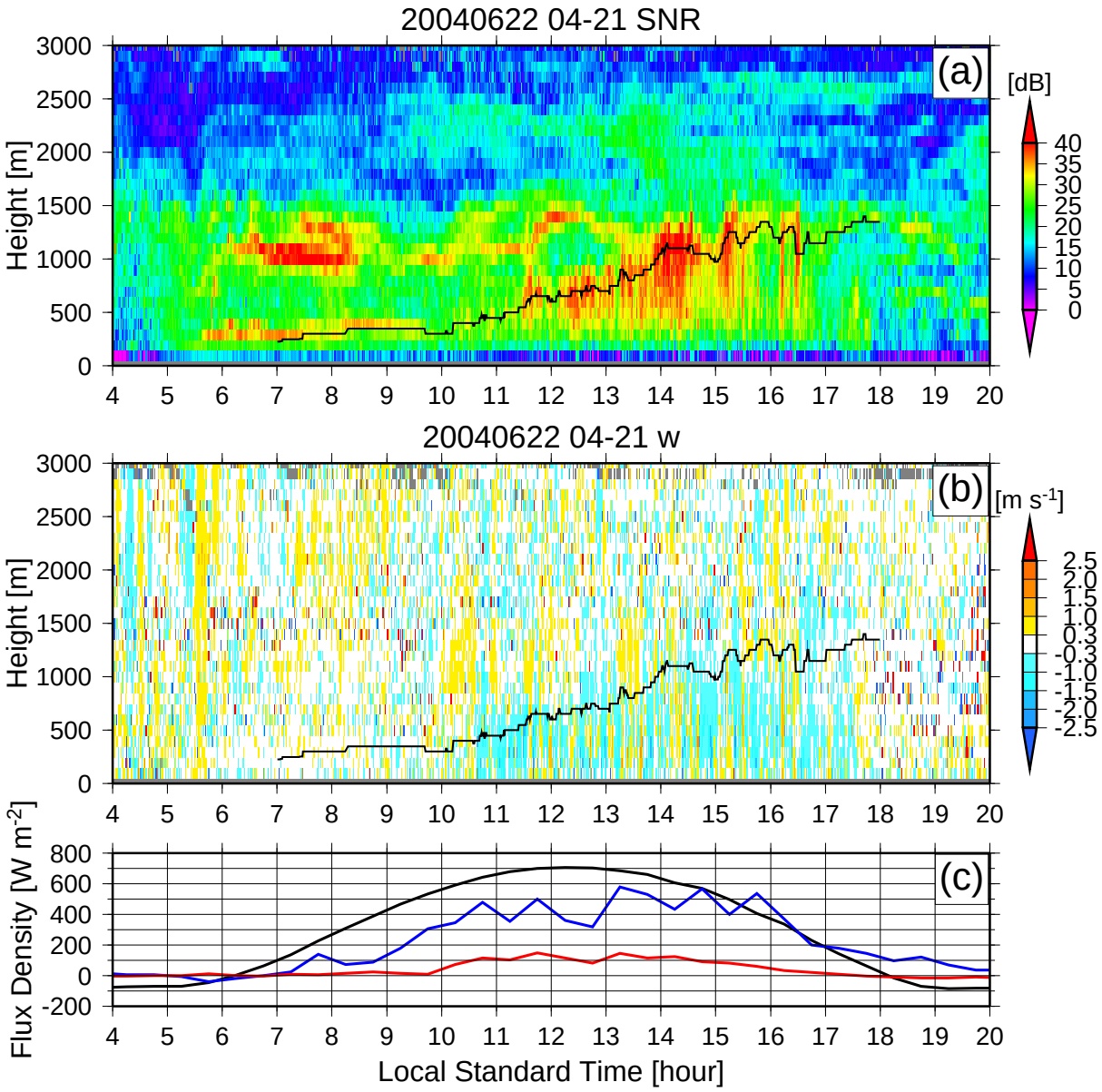

Fig. 9: The same as Fig. 8 but for 22 June 2004, referred to as the wet-case.

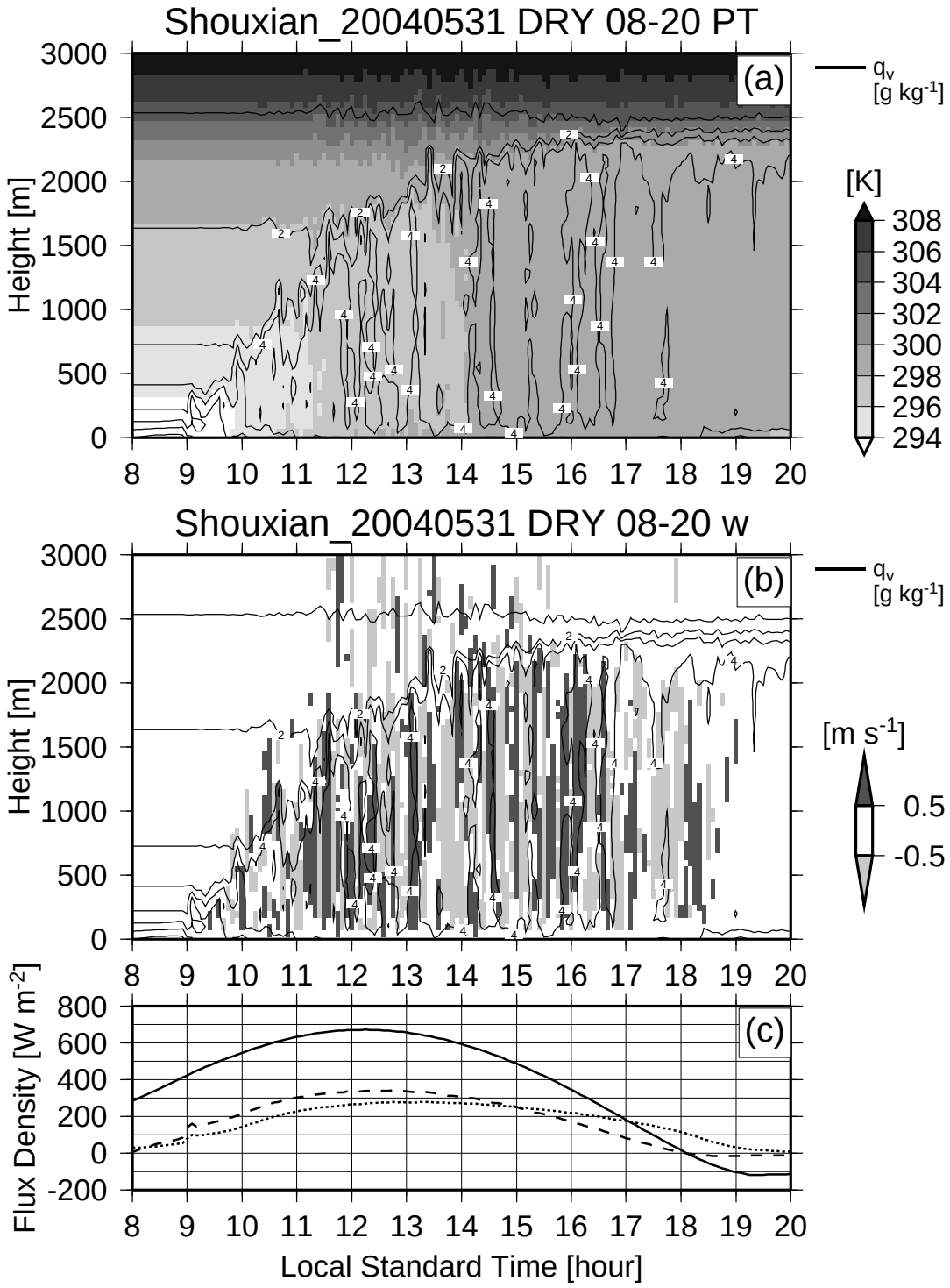

Fig. 10: (a) Time-height cross section of simulated potential temperature with the mixing ratio of water vapor (contours, every 1 g kg^{-1}) at the center of the model domain in the dry-case (31 May 2004). (b) The same as (a) but for vertical velocity. (c) Time series of net radiation (solid line), sensible heat flux (broken line), and latent heat flux (dotted line) averaged over the entire model surface.

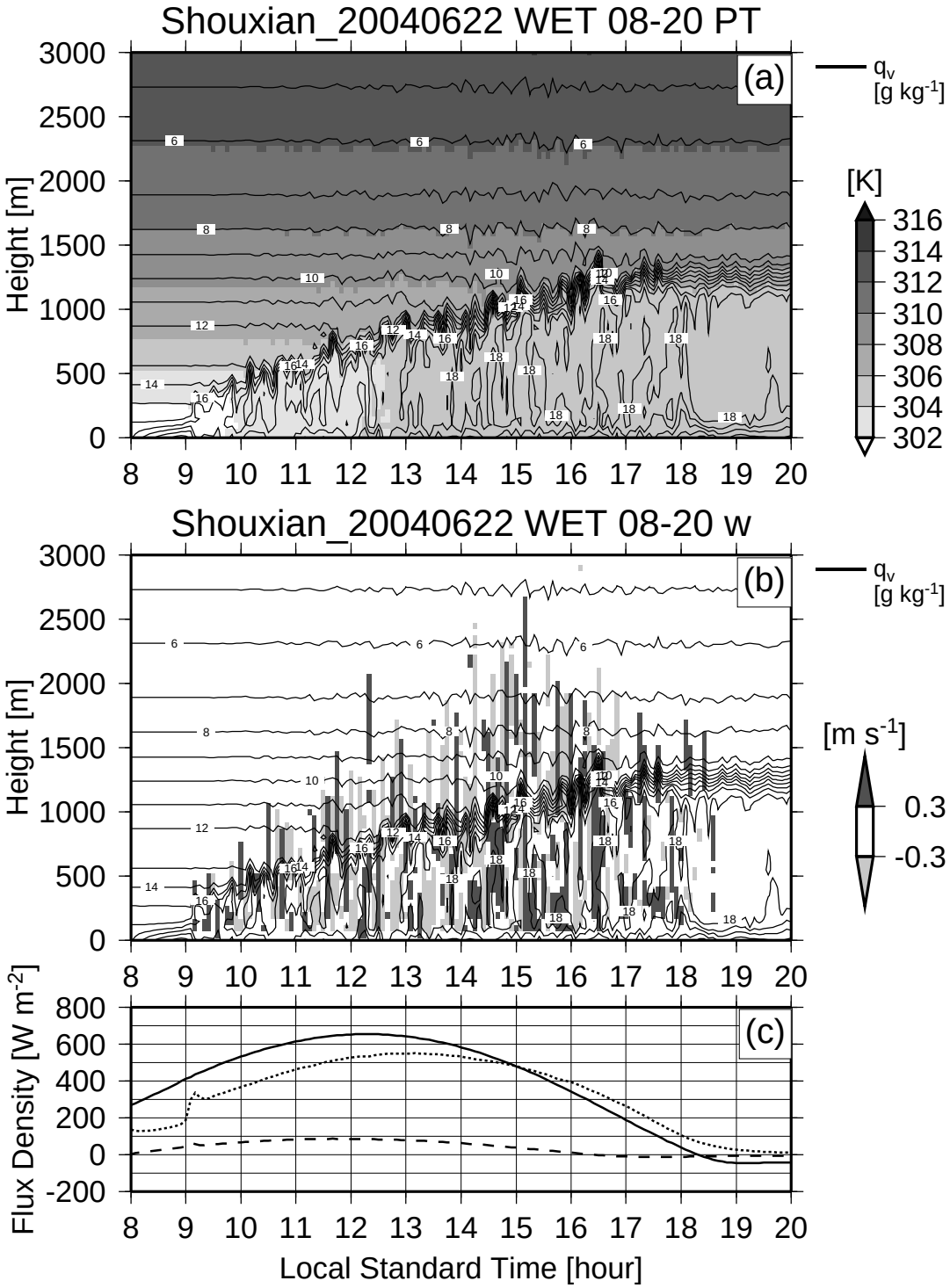

Fig. 11: The same as Fig. 10 but for the wet-case (22 June 2004).

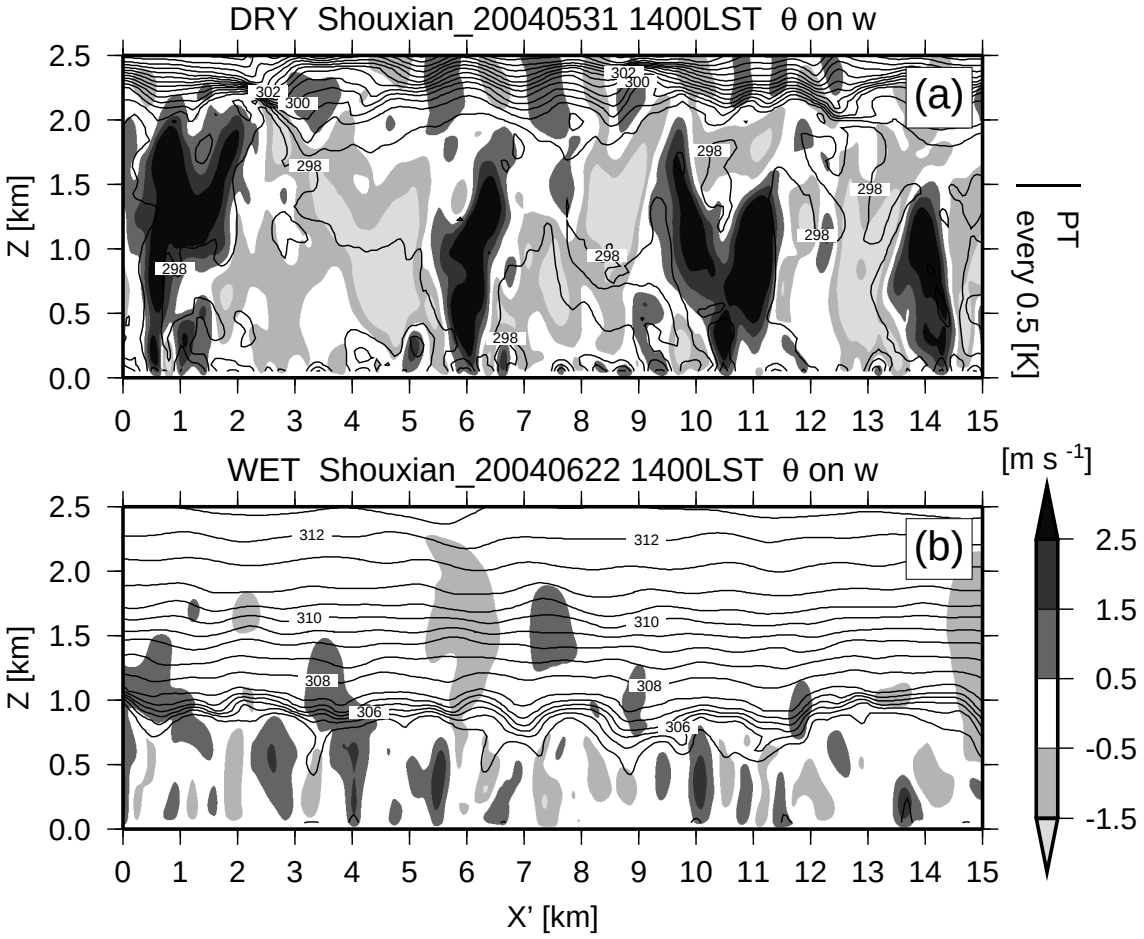

Fig. 12: Vertical cross section of simulated vertical velocity (shading) and potential temperature (contours, every 0.5 K) in a plane orthogonal to the mean horizontal wind at 14 LST for the dry-case (a) and the wet-case (b).

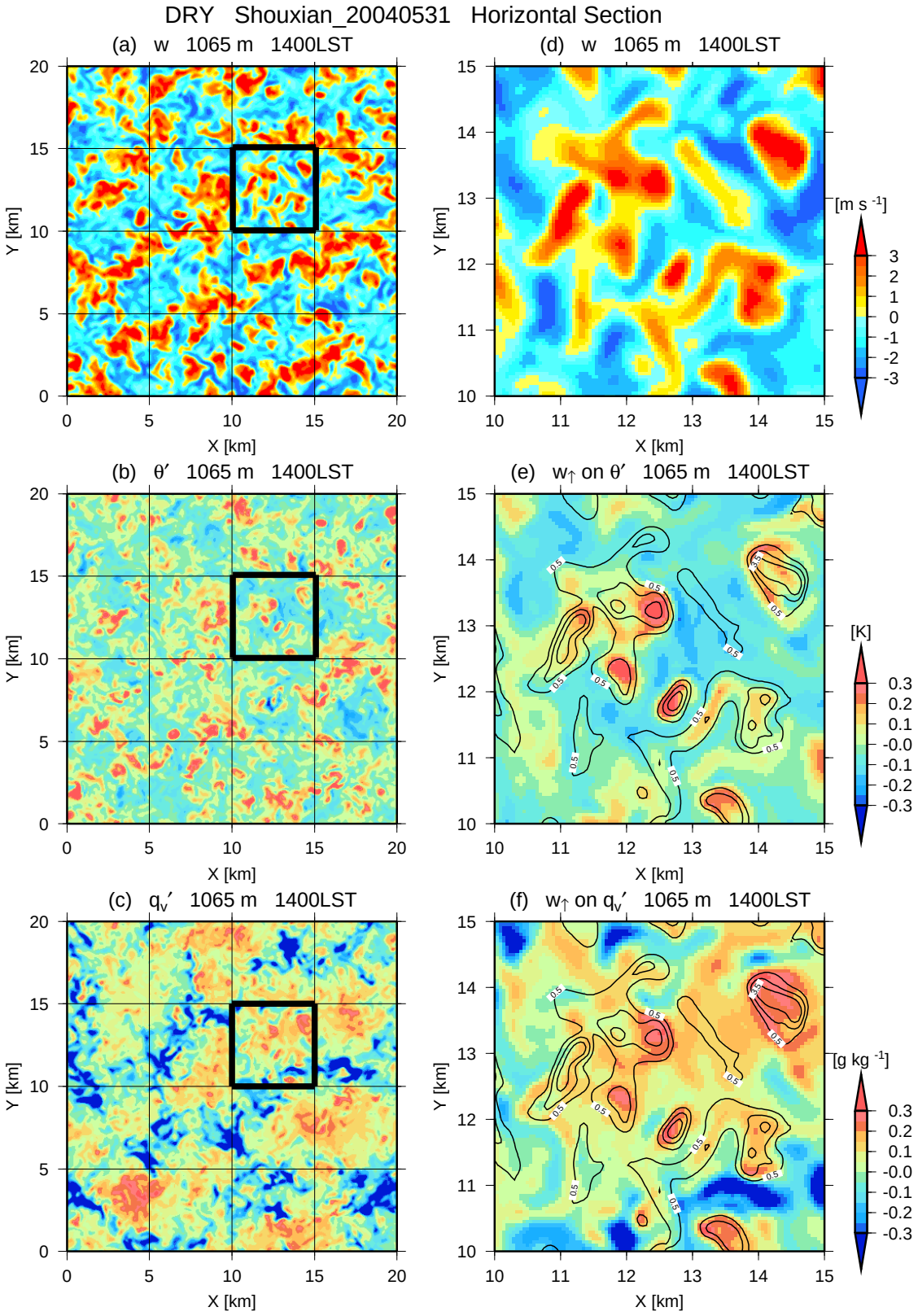

Fig. 13: Horizontal distribution of simulated vertical velocity (a, d), fluctuations of potential temperature (b, e), and the mixing ratio of water vapor (c, f) at a height of 1065 m ($z/z_i \sim 0.5$, where z_i is the height of the CBL top) at 14 LST in the dry-case. (a - c) show the whole model domain. (d - f) show close-up distributions in the areas outlined by black squares in (a - c). The contours indicate updraft over 0.5 m s^{-1} every 1.5 m s^{-1} (e, f).

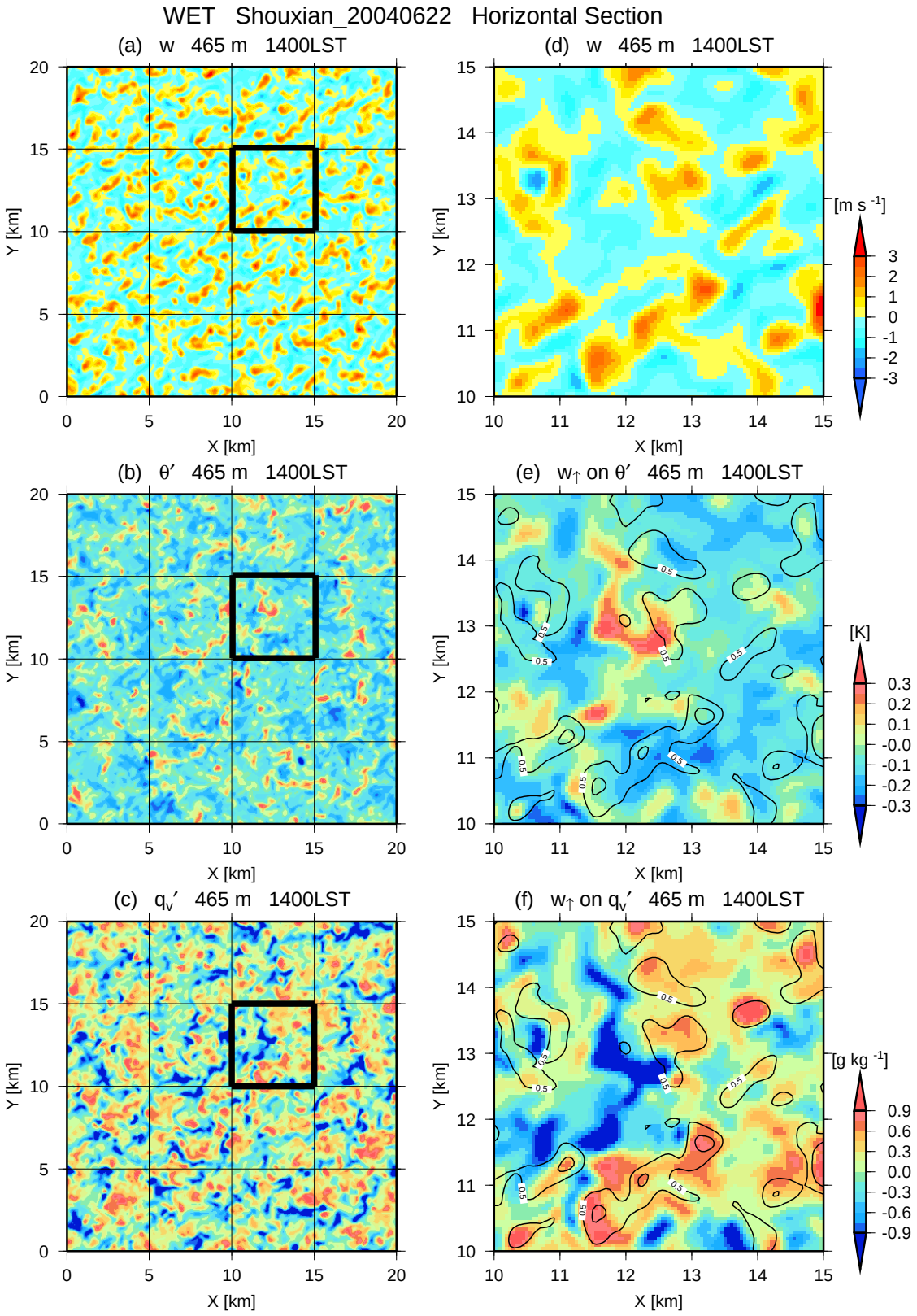

Fig. 14: The same as Fig. 13 but for a height of 465 m ($z/z_i \sim 0.5$) for the wet-case.

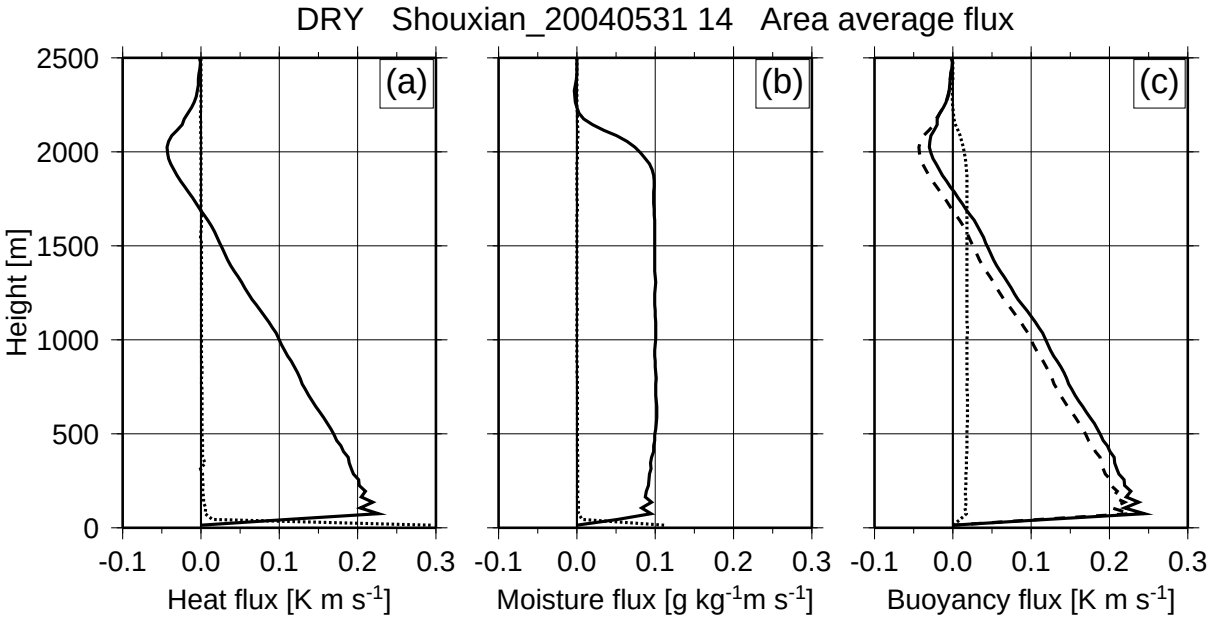

Fig. 15: (a) Profiles of resolved heat flux (solid line) and subgrid-scale (SGS) heat flux (dotted line) at 14 LST in the dry-case. (b) The same as (a) but for moisture flux. (c) Profiles of resolved buoyancy flux (solid line) and the contributions of heat (broken line) and of moisture (dotted line) to buoyancy flux.

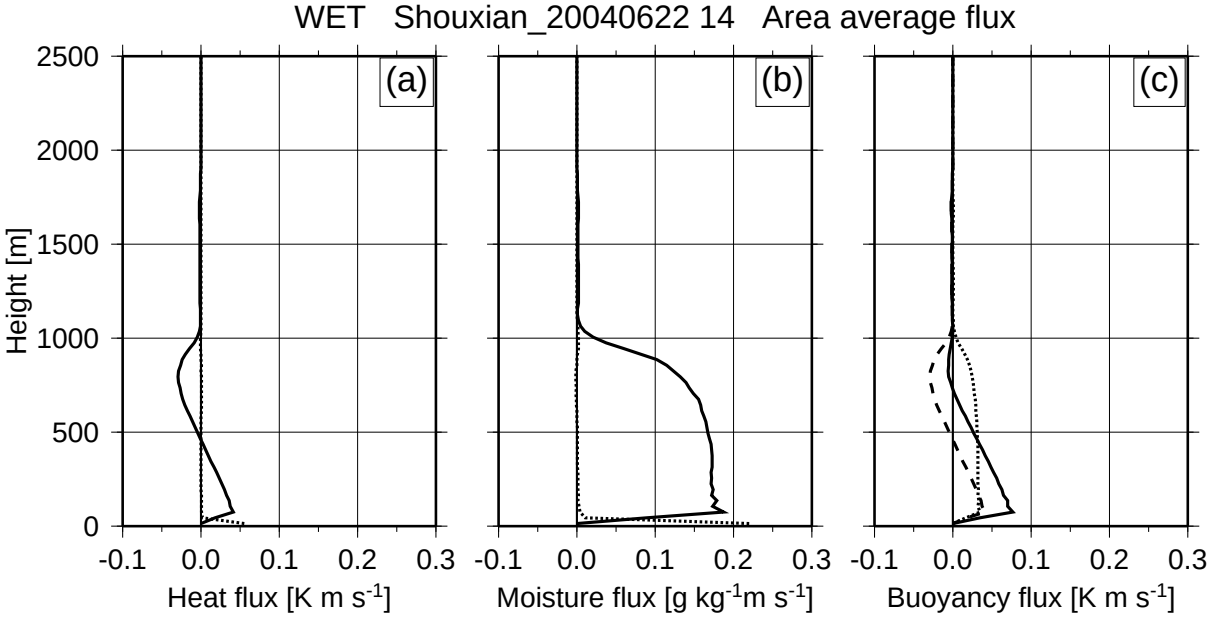

Fig. 16: The same as Fig. 15 but for the wet-case.

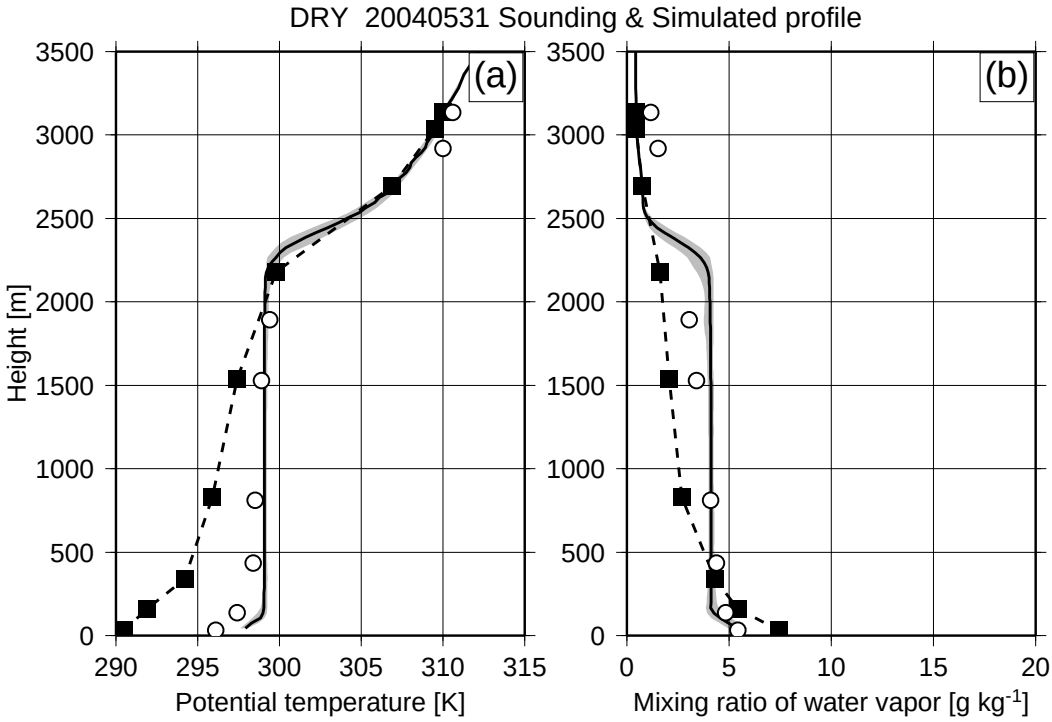

Fig. 17: (a) Profile of potential temperature obtained by sounding observations at Fuyang at 08 LST (solid squares) and 20 LST (open circles) on 31 May 2004 (the dry-case) and those by the simulation at 08 LST (initial condition; broken line) and 20 LST (solid line). The range between the maximal and minimal values is shaded. (b) The same as (a) but for the mixing ratio of water vapor.

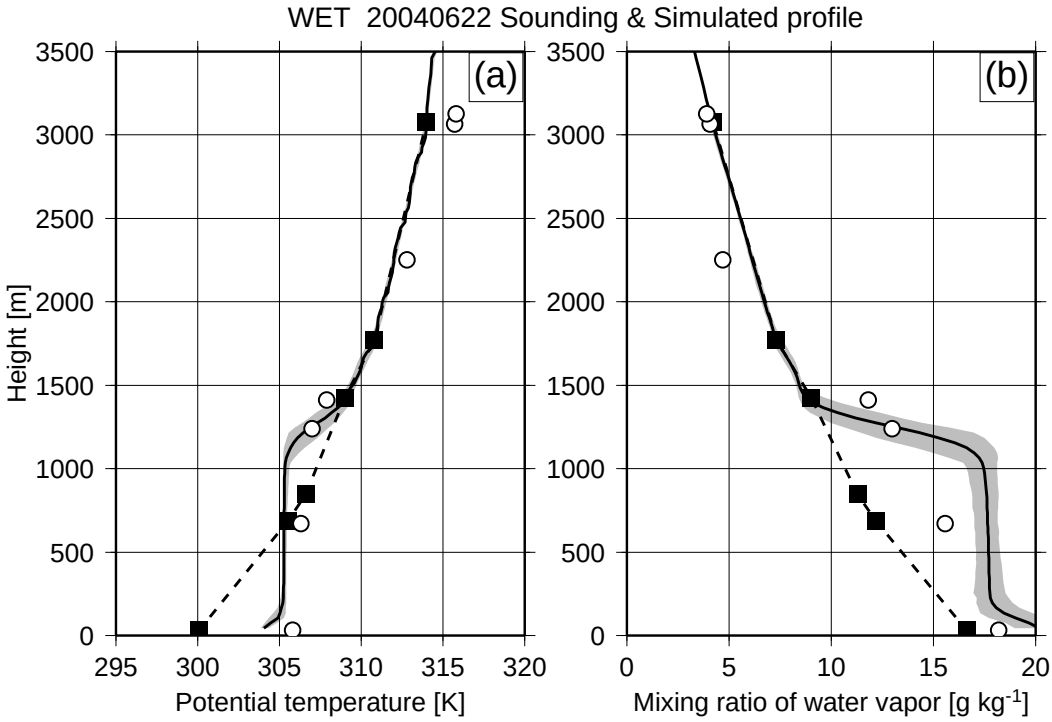

Fig. 18: The same as Fig. 17 but for 22 June 2004 (the wet-case).

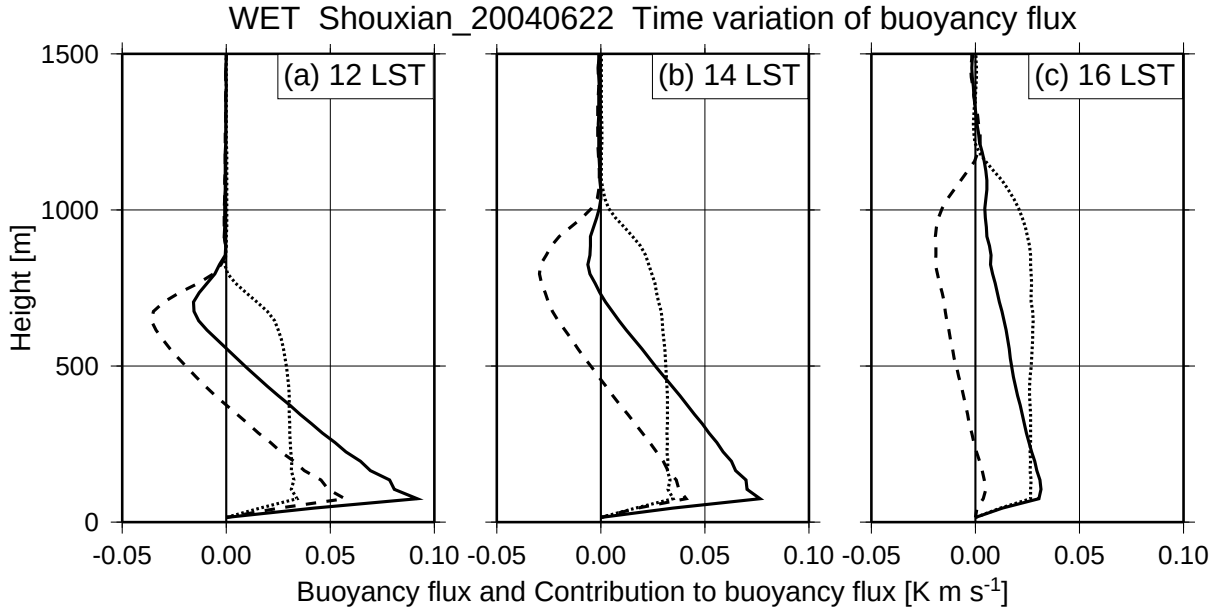

Fig. 19: Profiles of buoyancy flux (solid line) and the contributions of heat (broken line) and of moisture (dotted line) to buoyancy flux at 12 LST (a), 14 LST (b), and 16 LST (c) in the wet-case.

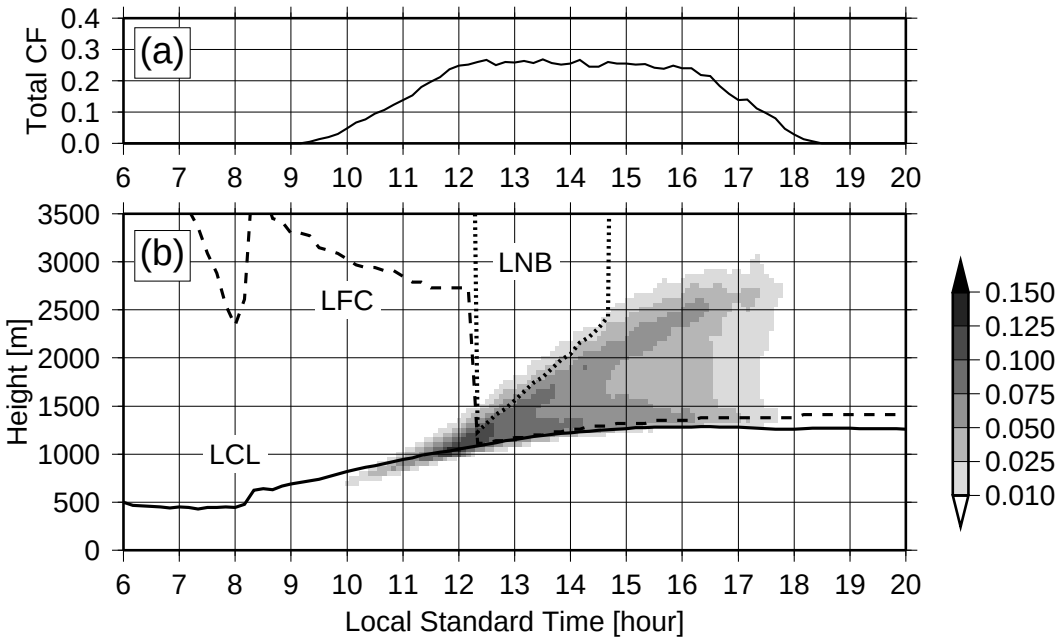

Fig. 20: (a) Time series of total cloud fraction. (b) Time-height cross section of cloud fraction and time series of LCL (solid line), LFC (broken line) and LNB (dotted line) calculated from mean values at 45 m height.

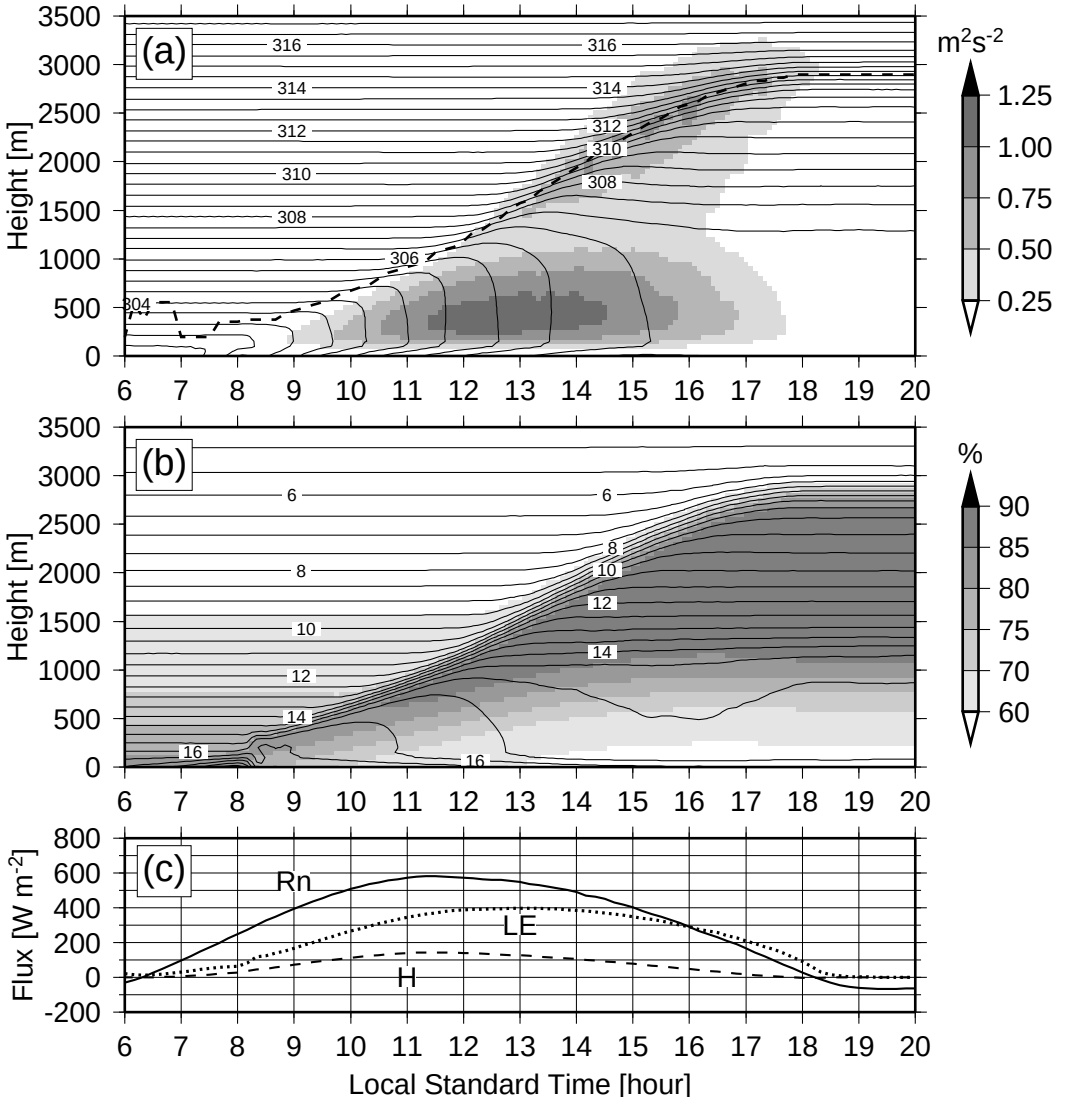

Fig. 21: (a) Time-height cross section of variance of vertical velocity (shading) with mean virtual potential temperature (contours, every 0.5 K). Broken line indicates the height of the maximum gradient of the virtual potential temperature. (b) The same as (a) but for mean relative humidity (shading) with mean water vapor mixing ratio (contours, every 0.5 g kg^{-1}). (c) Time series of surface net radiation flux (solid line), sensible heat flux (broken line) and latent heat flux (dotted line).

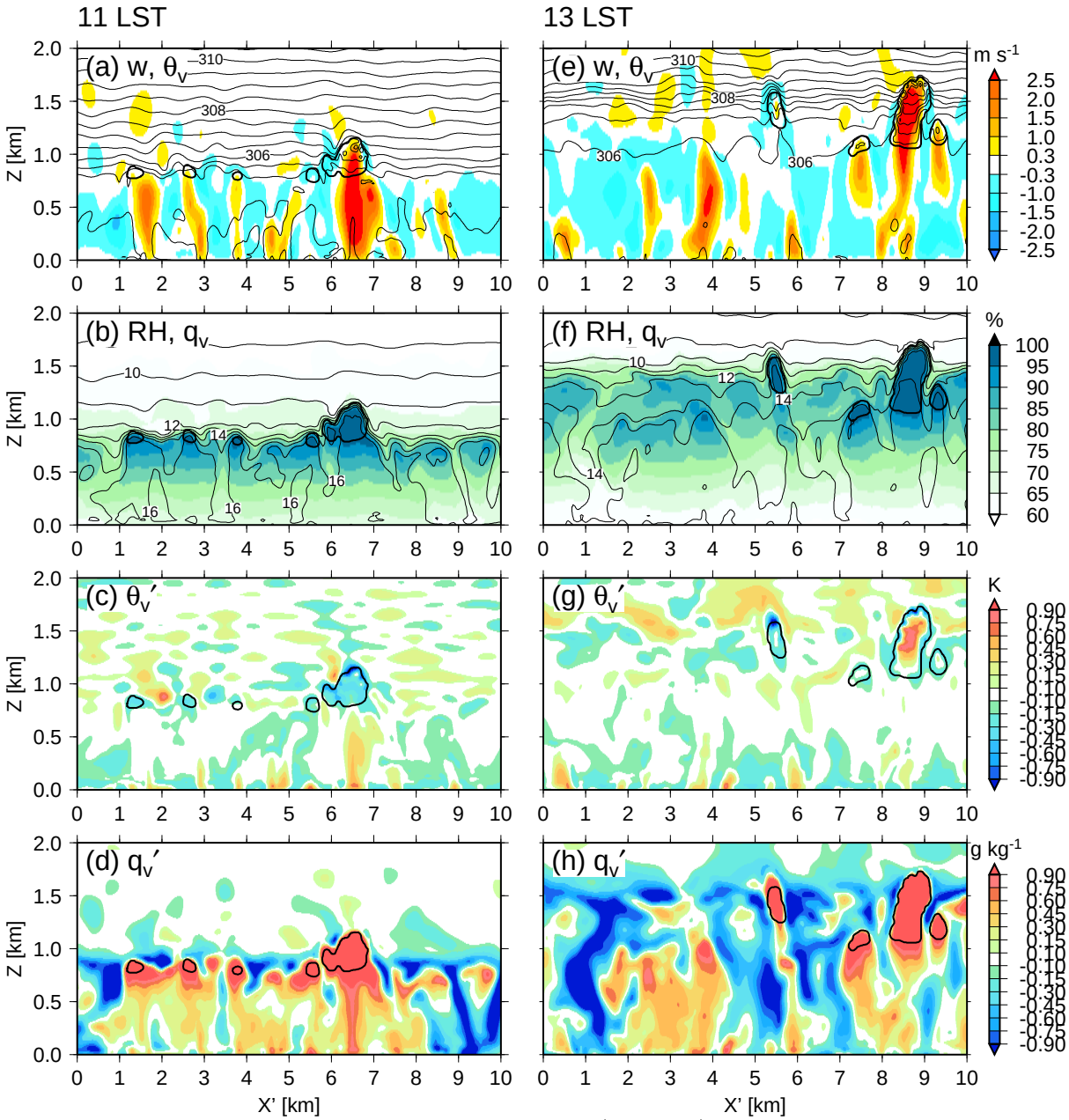

Fig. 22: Vertical cross section of vertical velocity (shading) with virtual potential temperature (contours, every 0.5 K) (a), relative humidity (shading) with water vapor (contours, every 1 g kg^{-1}) (b), perturbation of virtual potential temperature (c), and perturbation of water vapor mixing ratio (d) in a plane adjacent to the center of the model domain at 11 LST. Thick line indicates the cloud boundary defined by $q_c = 0.01$ g kg^{-1}. Panels (e) - (h) are the same as (a) - (d) but at 13 LST, respectively.

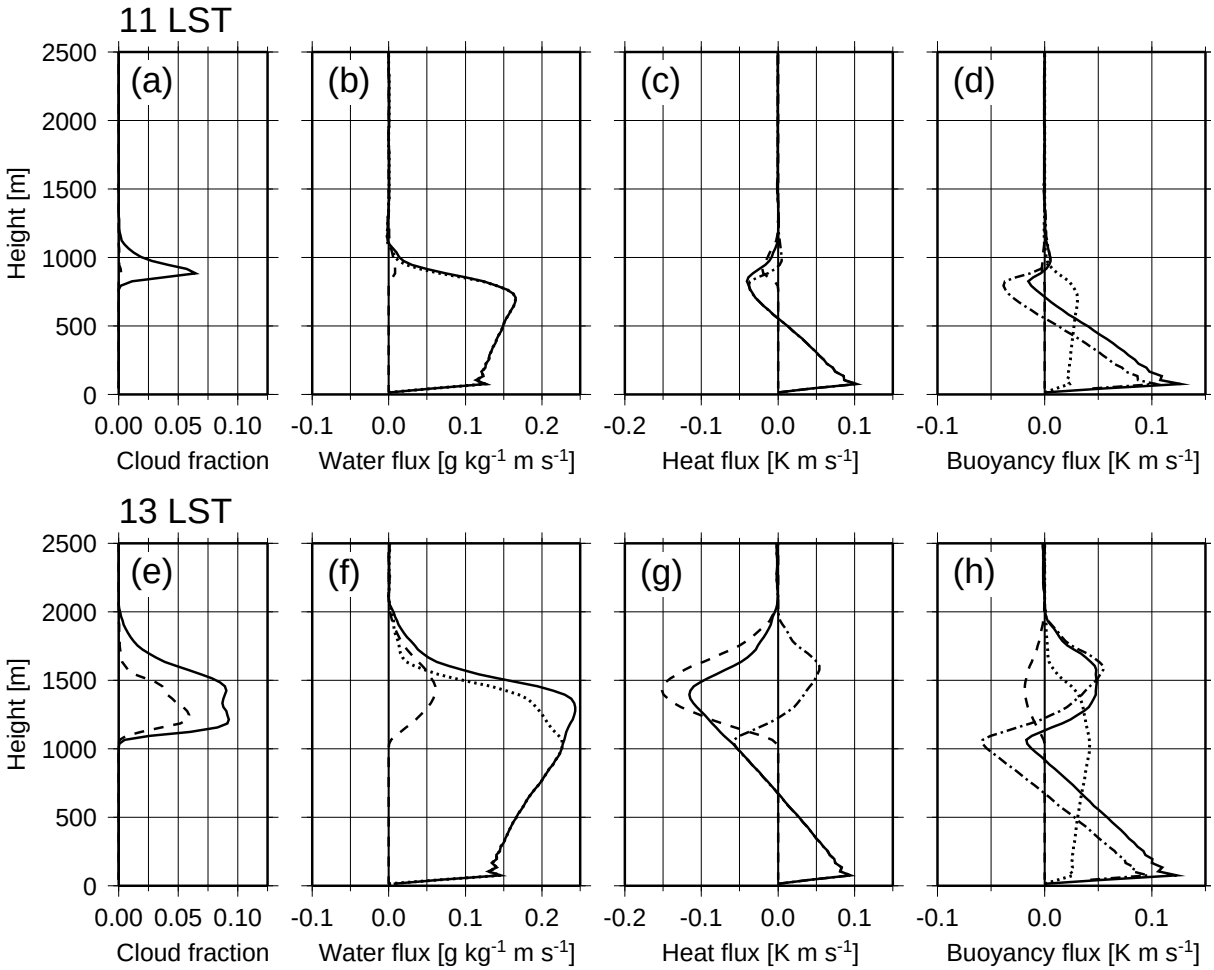

Fig. 23: Profiles of (a) cloud fraction (solid line), active cloud fraction ($q_c > 0$ and $\theta'_v > 0$; broken line), (b) total water flux ($\overline{w'q'_t}$; solid line), water vapor flux ($\overline{w'q'_v}$; dotted line), cloud water flux ($\overline{w'q'_c}$; broken line), (c) liquid water potential temperature flux ($\overline{w'\theta'_l}$; solid line), potential temperature flux (chain line) and contribution of liquid water flux (broken line) (d) virtual potential temperature flux ($\overline{w'\theta'_v}$; solid line), contribution of water vapor flux (dotted line), that of liquid water flux (broken line; nearly equal zero) and that of potential temperature flux (chain line) at 11 LST. Panels (e) - (h) are the same as (a) - (d) but at 13 LST, respectively.

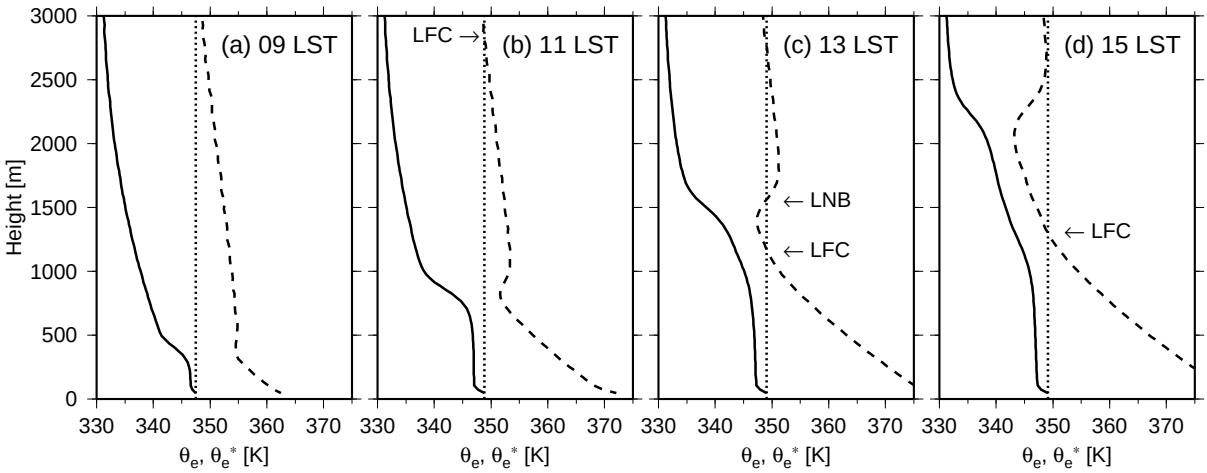

Fig. 24: Profiles of mean equivalent potential temperature (solid line) and saturated equivalent potential temperature (broken line) at 09 LST (a), 11 LST (b), 13 LST (c) and 15 LST (d), respectively. Dotted lines show the mean equivalent potential temperature of air near the land surface (45 m height).

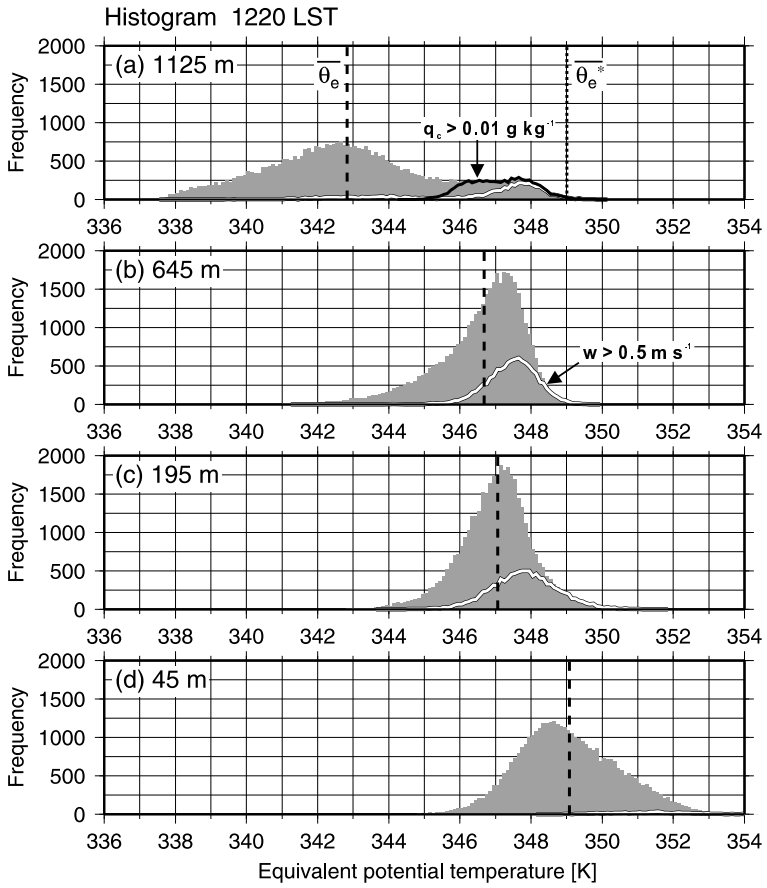

Fig. 25: Histogram of equivalent potential temperature θ_e at 1220 LST at the height of 1125 m: the height of the local minimum of mean saturated equivalent potential temperature $\overline{\theta_e^*}$ (a), 645 m (b), 195 m (c) and 45 m (d), respectively. Broken and dotted lines indicate $\overline{\theta_e}$ and $\overline{\theta_e^*}$, respectively. Black and white solid lines represent θ_e satisfying the condition of cloud water $q_c > 0.01$ g kg^{-1} and vertical velocity $w > 0.5$ m s^{-1}, respectively.

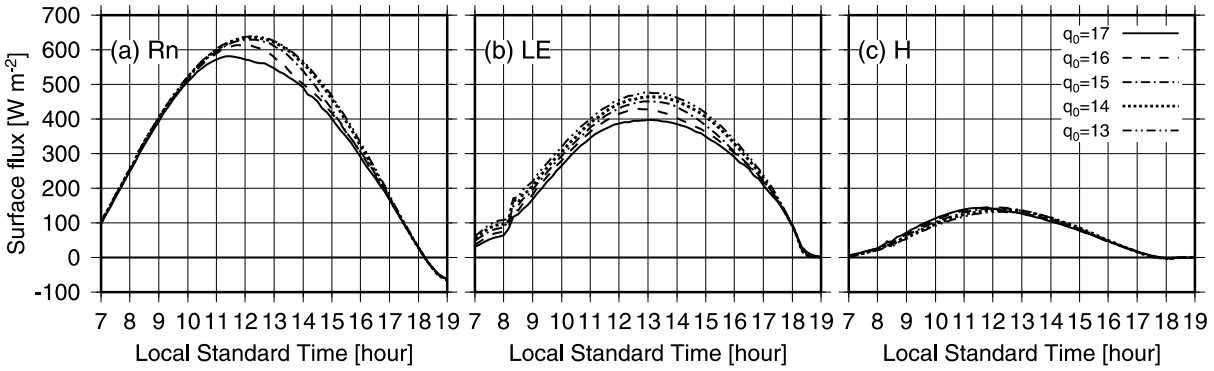

Fig. 26: Time series of surface net radiation flux (a), latent heat flux (b) and sensible heat flux (c) for the sensitivity simulations for the initial amount of water vapor.

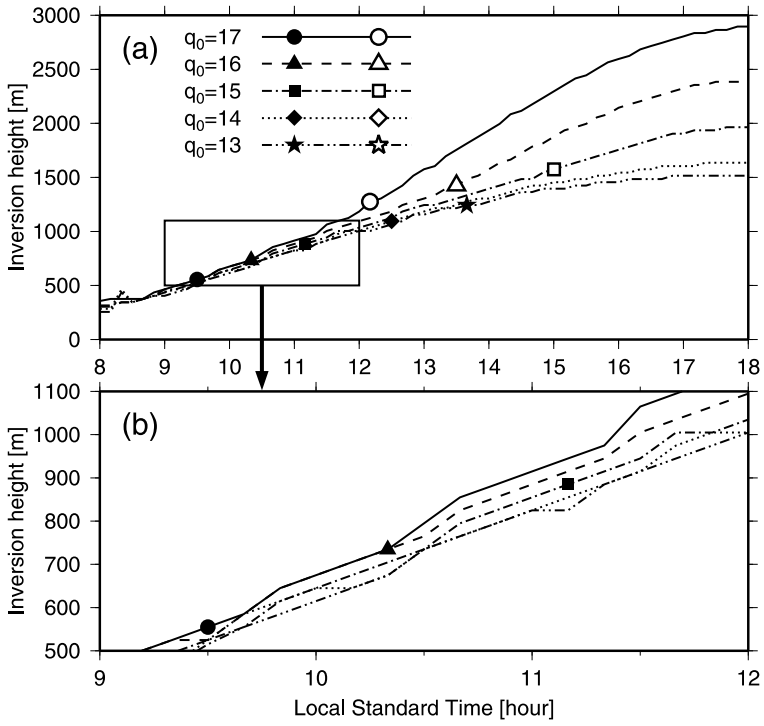

Fig. 27: (a) Time series of the inversion height for the sensitivity simulations for the initial amount of water vapor. Black symbols on each line indicate the time that total cloud fraction excess 0.01 (corresponging to the forced cumulus onset). White symbols on each line indicate the time that LFC decreased below the inversion height (corresponding to the active cumulus onset). (b) Close-up view in the area outlined by rectangle in (a).

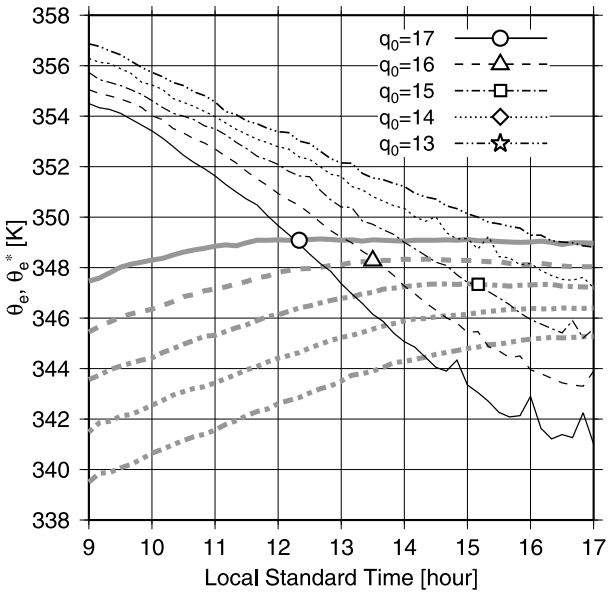

Fig. 28: Time series of mean equivalent potential temperature near the land surface (45 m height) $\overline{\theta_e(z_s)}$ (gray lines) and the mean saturated equivalent potential temperature at the height of the minimum of enthalpy flux (corresponging to the bottom of the inversion layer) $\overline{\theta_e^*(z_{ib})}$ (black lines). Intersection points of the gray and white lines (white symbols) correspond to the active cumulus onset time same as Fig. 27.

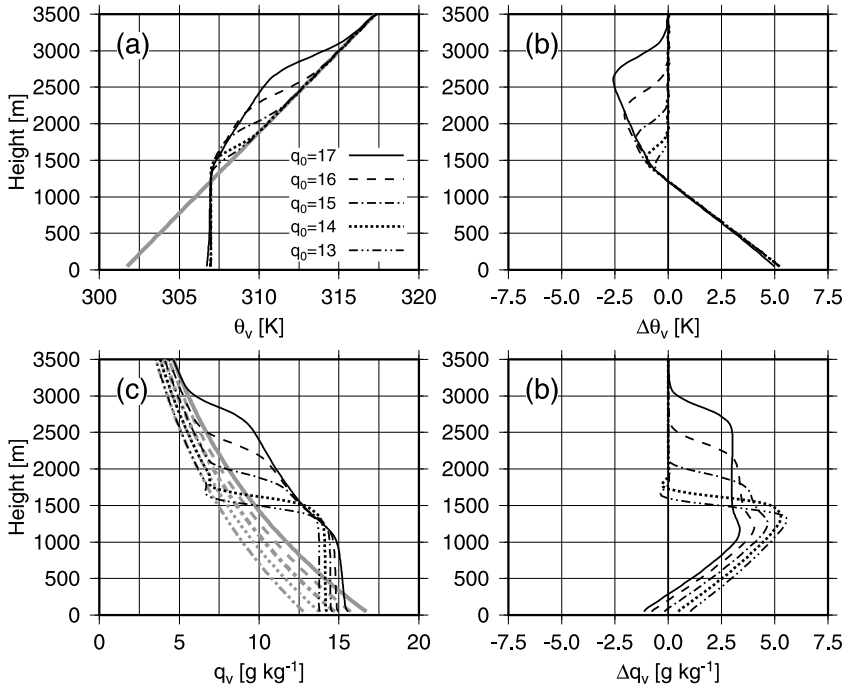

Fig. 29: (a) Profiles of mean virtual potential temperature at 06 LST (gray lines) and 19 LST (black lines) for the sensitivity simulations for the initial amount of water vapor. (b) Profiles of the differences between mean virtual potential temperature at 06 LST and those at 19 LST. (c), (d) The same as (a) and (b) except for mixing ratio of water vapor.

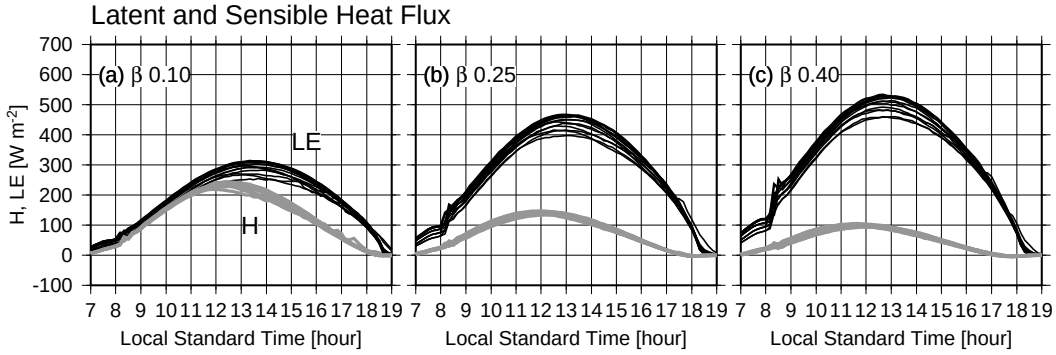

Fig. 30: Time series of surface latent heat flux (black lines) and sensible heat flux (gray lines) in the sensitivity simulations for the evaporative efficiency for $\beta = 0.10$ (a), 0.25 (b) and 0.40 (c). Each panel shows the results of 12 simulations for different initial amount of water vapor and strength of stratification.

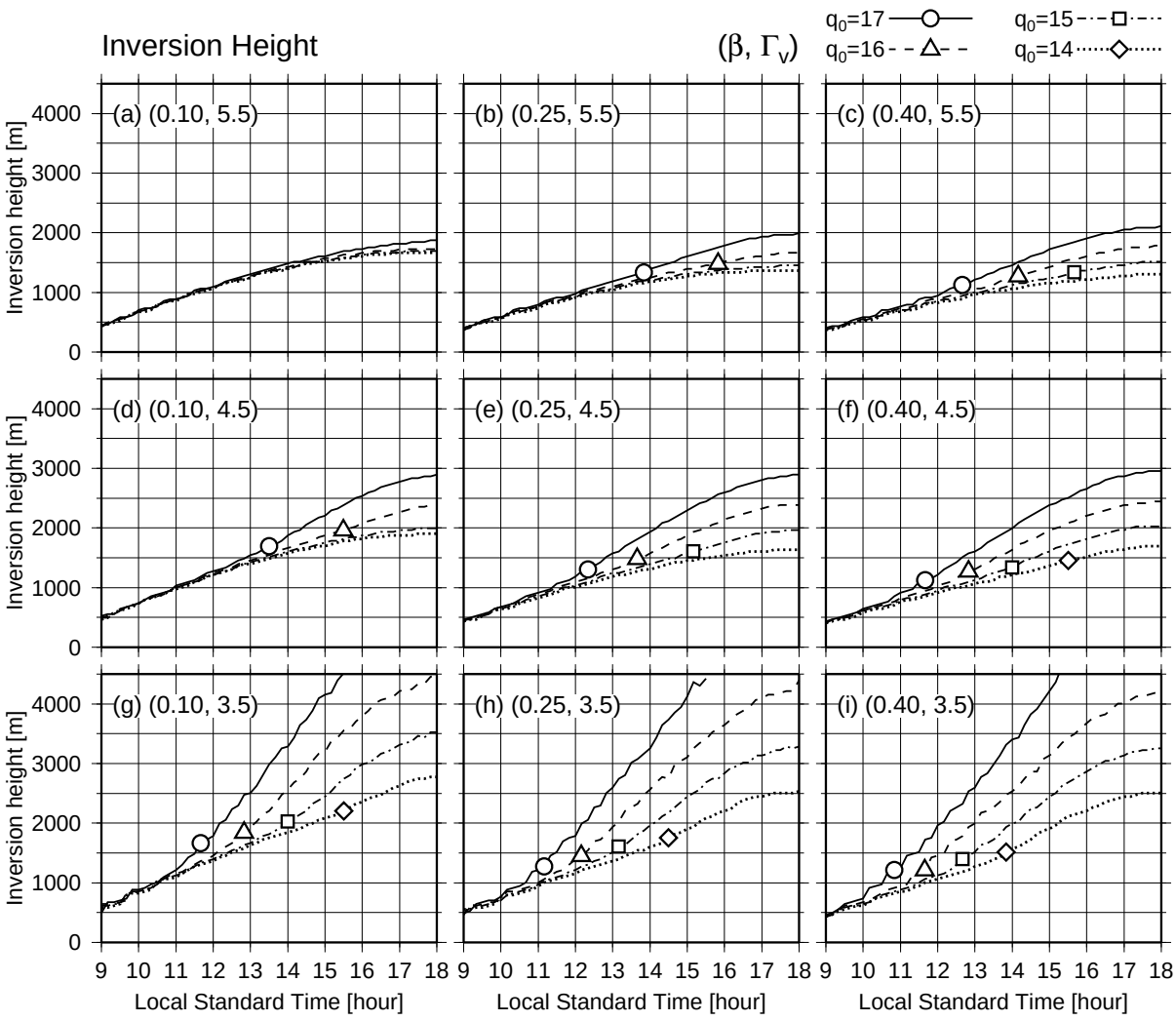

Fig. 31: Time series of the inversion heights in the sensitivity simulations. Each panel shows results of 4 simulations using the different initial amount of water vapor (q_0) and same evaporative efficiency and strength of stratification (β, Γ_v). White symbols on each line indicate the time that LFC decreased below the inversion height (corresponding to the active cumulus onset). The panel (e) are same as those in Fig 27 except for without the simulations for $q_0 = 13$ g kg^{-1}. Simulations for $q_0 = 17$ g kg^{-1} in panel (g)-(i) are shown until 1530 LST.

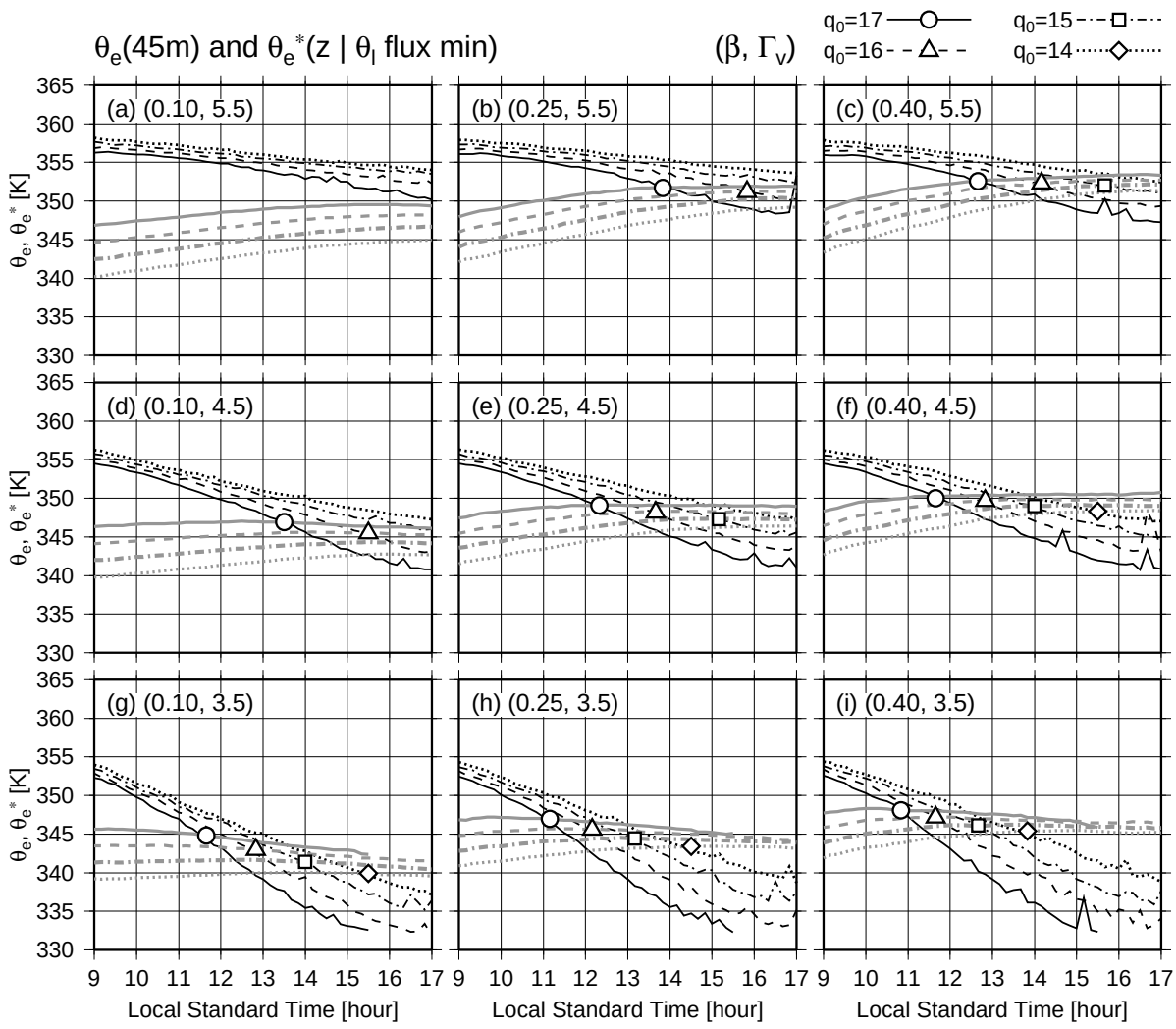

Fig. 32: The same as Fig. 31 except for mean equivalent potential temperature near the land surface $\overline{\theta_e(z_s)}$ (gray lines) and the mean saturated equivalent potential temperature at the bottom height of the inversion layer $\overline{\theta_e^*(z_{ib})}$ (black lines). White symbols on each line correspond to the active cumulus onset same as Fig. 31.

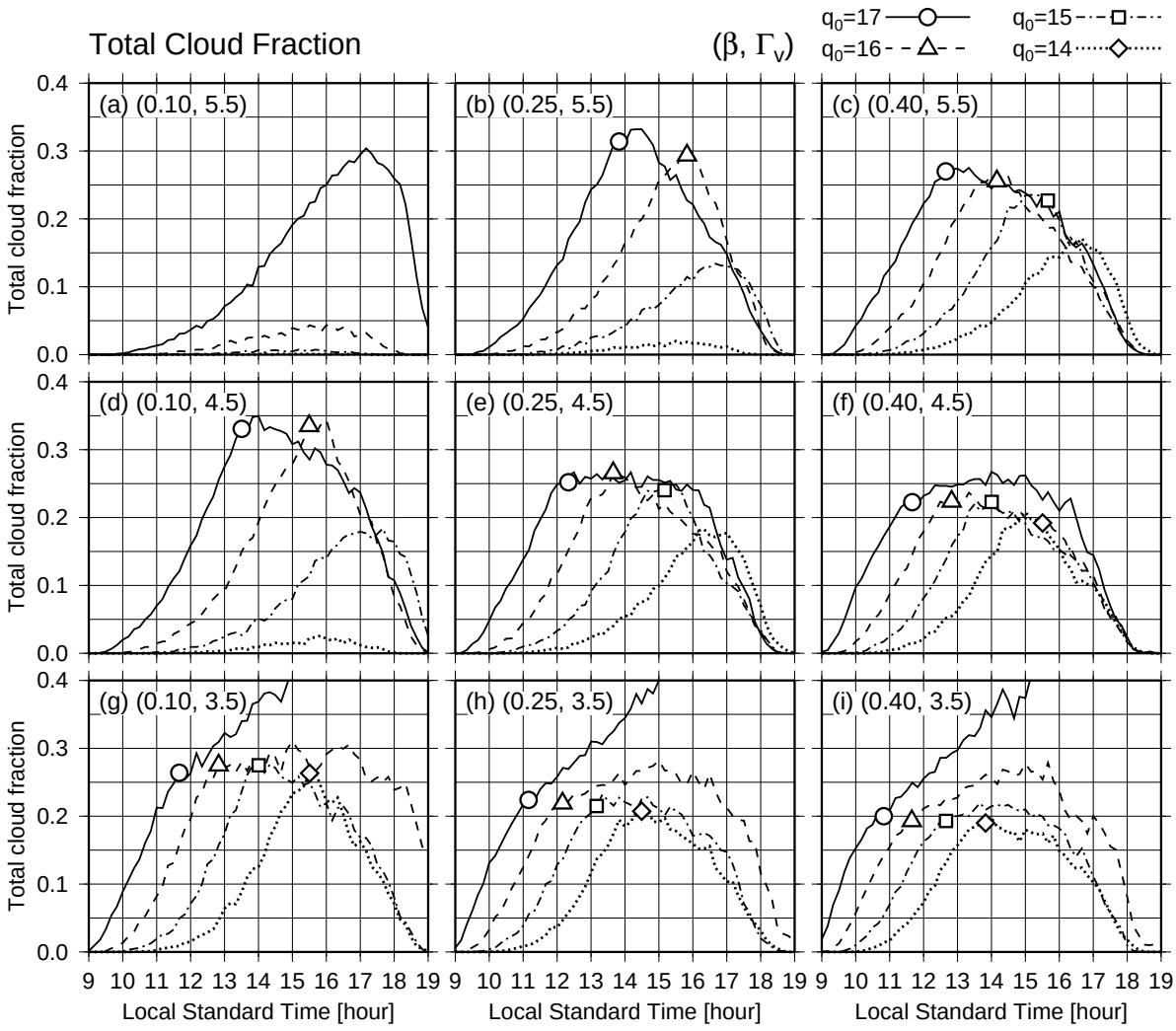

Fig. 33: The same as Fig. 31 except for total cloud fraction.

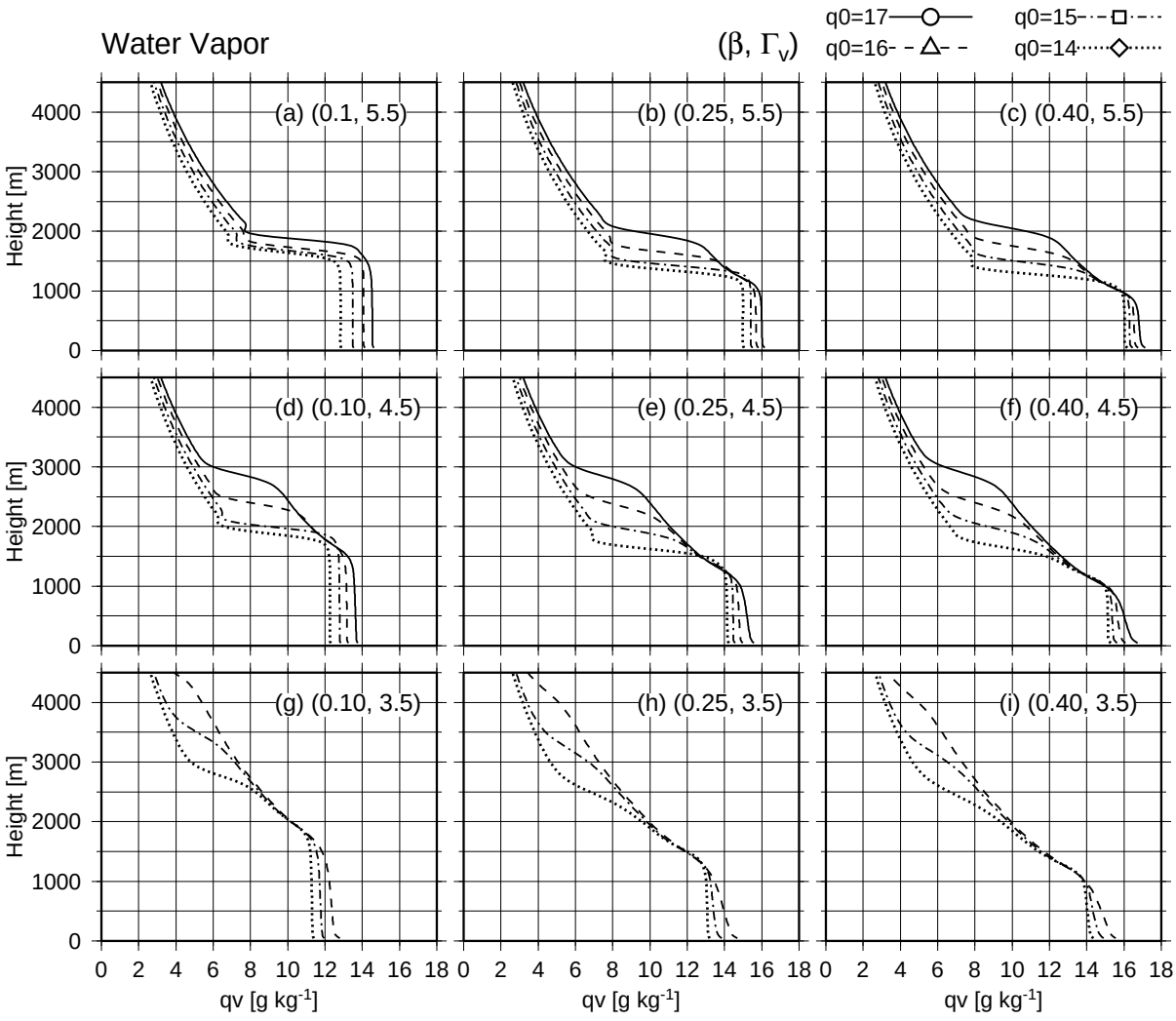

Fig. 34: The same as Fig. 31 except for the mixing ratio of water vapor at 19 LST. Simulations for $q_0 = 16$ g kg^{-1} in panels (g) - (i) are not shown.

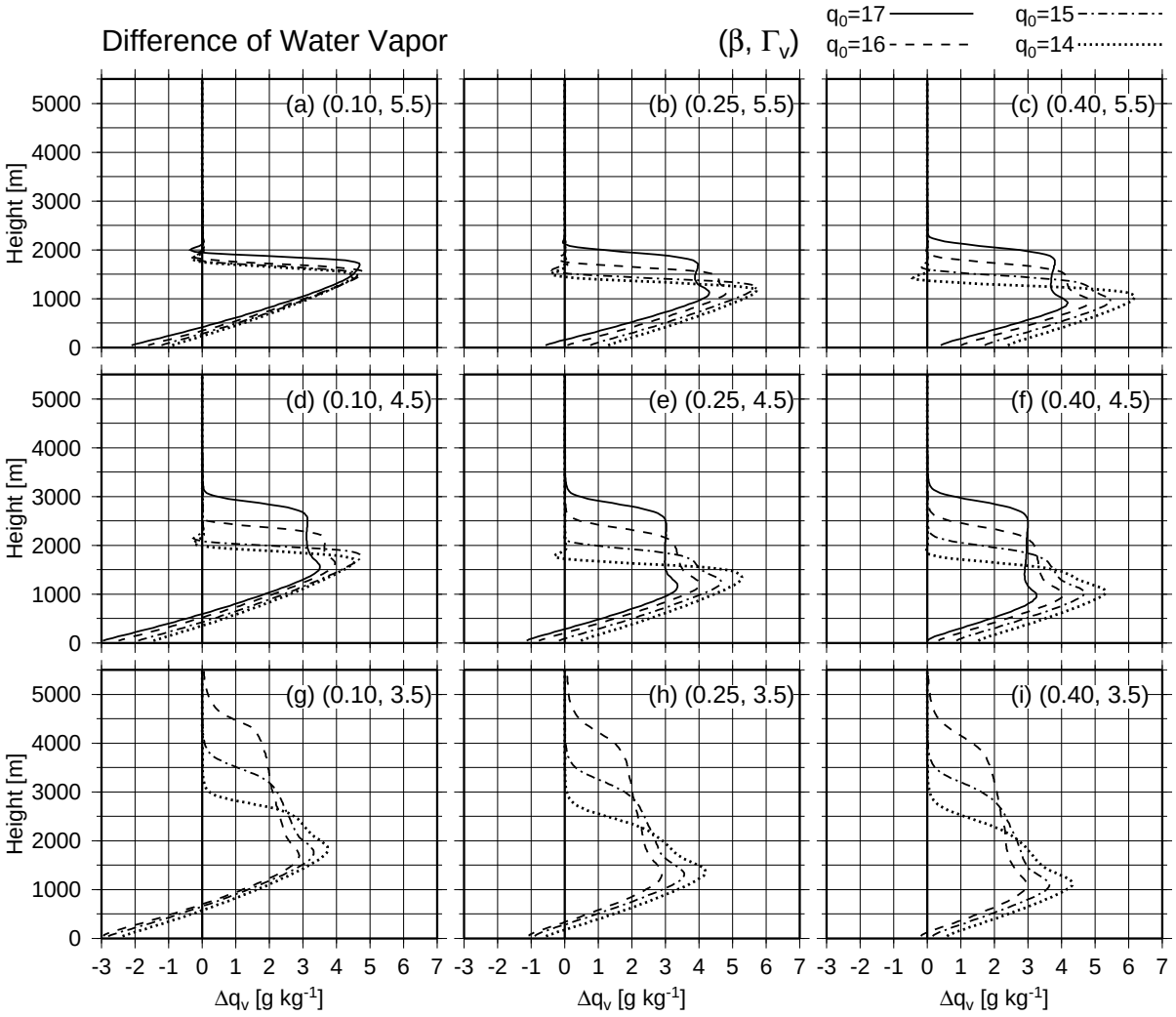

Fig. 35: The same as Fig. 31 except for the difference between mixing ratio of water vapor at 06 LST and that at 19 LST. Simulations for $q_0 = 16$ g kg^{-1} in panels (g) - (i) are not shown.

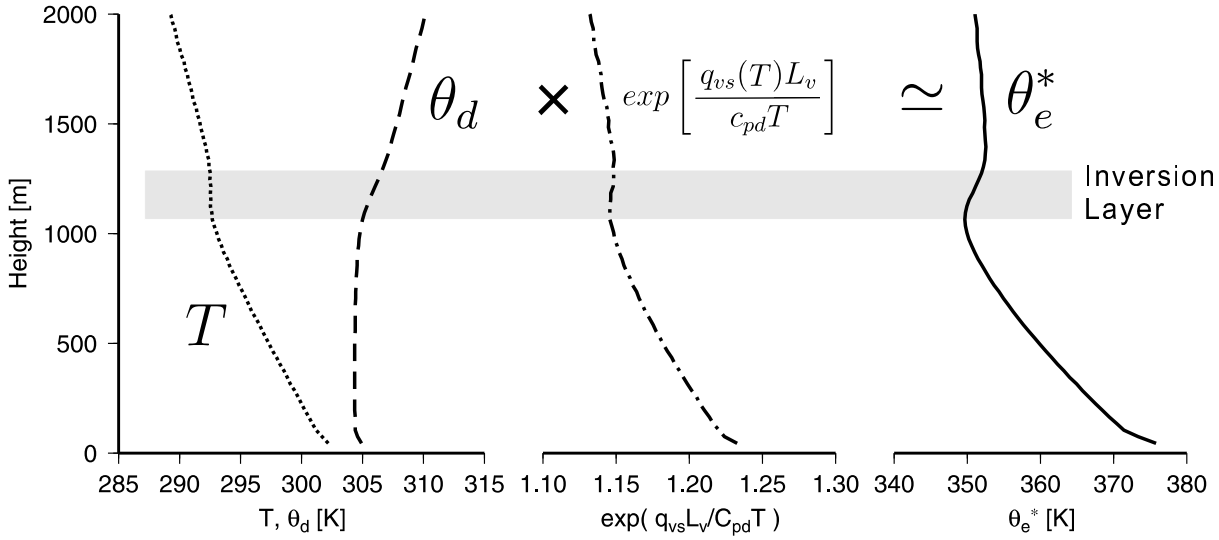

Fig. 36: Mean profiles of saturated equivalent potential temperature (solid line) and its components; temperature (dotted line), dry potential temperature (broken line) and $\exp(q_{vs}L_v/c_{pd}T)$ (chain line) at 12 LST.